

Fragmentation in the Massive Star-Forming Region IRAS 19410+2336[★]

J. A. Rodón¹, H. Beuther², and P. Schilke³

¹ European Southern Observatory, Alonso de Córdova 3107, Vitacura, Casilla 19001, Santiago 19, Chile.
e-mail: jrodon@eso.org

² Max-Planck-Institut für Astronomie, Königstuhl 17, 69117 Heidelberg, Germany.

³ I. Physikalisches Institut, Universität zu Köln, Zùlpicherstr. 77, 50937 Köln, Germany.

Received ; accepted

ABSTRACT

Context. The Core Mass Functions of low-mass star-forming regions are found to resemble the shape of the Initial Mass Function (IMF). A similar result is observed for the dust clumps in high-mass star forming regions, although at spatial scales of clusters that do not resolve the substructure that is found in these massive clumps. The region IRAS 19410+2336 is one exception, having been observed at spatial scales on the order of ~ 2500 AU, sufficient to resolve the clump substructure into individual cores.

Aims. We investigate the protostellar content of IRAS 19410+2336 at high spatial resolution at 1.4 mm, determining the temperature structure of the region and deriving its Core Mass Function.

Methods. The massive star-forming region IRAS 19410+2336 was mapped with the PdBI (BCD configurations) at 1.4 mm and 3 mm in the continuum and several transitions of formaldehyde (H_2CO) and methyl cyanide (CH_3CN). The H_2CO transitions were also observed with the IRAM 30 m Telescope.

Results. We detected 26 continuum sources at 1.4 mm with a spatial resolution down to ~ 2200 AU, several of them with counterparts at NIR and MIR wavelengths, distributed in two (proto)clusters. With the PdBI CH_3CN and PdBI/IRAM 30 m H_2CO emission we derived the temperature structure of the region, ranging from 35 to 90 K. Using these temperatures we calculated the core masses of the detected sources, ranging from ~ 0.7 to $\sim 8 M_\odot$. These masses were strongly affected by the spatial filtering of the interferometer, filtering out a common envelope with $\sim 90\%$ of the single-dish flux. Considering only the detected dense cores, and accounting for binning effects as well as cumulative distributions, we derived a Core Mass Function, with a power-law index $\beta = -2.3 \pm 0.2$. We resolve the Jeans length of the (proto)clusters by one order of magnitude, and only find little velocity dispersion between the different substructures.

Conclusions. Since we cannot unambiguously differentiate protostellar and prestellar cores, the derived CMF is not prestellar. Furthermore, because of the large fraction of missing flux, we cannot establish a firm link between the CMF and the IMF. This implies that future high-mass CMF studies will require to complement the interferometer continuum data with the short spacing information, a task suitable for ALMA. We note that the method of extracting temperatures using H_2CO lines becomes less applicable when reaching the dense core scales of the interferometric observations because most of the H_2CO appears to originate in the envelope structure.

Key words. stars: formation – instrumentation: high angular resolution – instrumentation: interferometers – ISM: individual objects: IRAS 19410+2336

1. Introduction

Our understanding of the structure of the cold, dense interstellar medium (ISM) in star-forming regions has improved in the last years. In those regions the ISM exhibits a clumpy, often filamentary structure with density maxima at the sites of star formation. To represent this structure quantitatively we use the Core Mass Function (CMF). In this paper we will refer to “core” as the small (diameter $D \sim 0.01$ pc), dense condensation that will form individual stars or small multiple systems, while with “clump” we denote structures that may form (proto)clusters and may therefore be more massive and larger than cores. In this sense, cores may be considered as a subset of clumps.

Sub-mm observations of low-mass star-forming regions such as Serpens (e.g., Testi & Sargent 1998), Orion B (e.g.,

Motte et al. 2001), Aquila (e.g., Könyves et al. 2010) and ρ Oph (e.g., Motte et al. 1998), as well as near-infrared extinction maps (e.g., Alves et al. 2007), show that their CMFs resemble the shape and intrinsic mass scale of the stellar initial mass function (IMF; e.g., Salpeter 1955; Kroupa 2002). This suggests that these dense cores would be the immediate precursors of stars, and that by applying a more or less constant core-to-star mass conversion efficiency we can obtain the IMF from the CMF.

In the case of Massive Star-Forming (MSF) regions we have, for example, the analysis of Reid & Wilson (2006). They gathered the published masses of the MSF regions M8 (e.g., Tothill et al. 2002), M17 (e.g., Reid & Wilson 2006), NGC 7538 (e.g., Reid & Wilson 2005), W43 (e.g., Motte et al. 2003) and RCW 106 (e.g., Mookerjee et al. 2004), tracing spatial scales of clumps that correspond to (proto)clusters rather than to individual cores, and tested the fit of several functional forms for their clump mass functions. They found that in those cases, the best fit was obtained by a double power law, having a mean power-

[★] Based on observations carried out with the IRAM Plateau de Bure Interferometer and the IRAM 30m Telescope. IRAM is supported by INSU/CNRS (France), MPG (Germany) and IGN (Spain)

law exponent for the high-mass end consistent with the Salpeter IMF. This would again imply that by an almost one-to-one mass conversion efficiency the IMF could be obtained from the clump mass function, as in the case for low-mass star-forming regions. Similar analysis were conducted by e.g., Shirley et al. (2003); Beltrán et al. (2006). Furthermore, a theoretical study by Chabrier & Hennebelle (2010) on the relationship between the CMF and the IMF suggests a tight correlation between the two. Once more, this implies that the IMF would be defined by the CMF in the early stages of evolution.

However, this one-to-one relationship may not hold as, for example, some clumps must fragment to produce the observed quantity of multiple stellar systems (Goodwin et al., 2007). The relatively large distances ($\gtrsim 2$ kpc) of most of the known MSF regions require a spatial resolution of about $1''$ to resolve the clumps into cores with sizes below ~ 0.1 pc. That resolution in the (sub)mm regime is only achievable with the interferometric technique. So far, only a few MSF regions have been observed in the (sub)mm with spatial resolutions good enough to resolve individual cores (e.g., Bontemps et al. 2010, Fontani et al. 2009, Rodón et al. 2008, Rathborne et al. 2008, Beuther et al. 2006), and only for one source, IRAS 19410+2336, has it been possible to determine a core mass function (Beuther & Schilke, 2004).

The young MSF region IRAS 19410+2336 is at a distance of 2.16 kpc (Xu et al., 2009) and has an integrated bolometric luminosity of about $10^4 L_{\odot}$. It is a very active star-forming site, with sources detected from X-rays down to radio wavelengths. It has H_2O and CH_3OH maser emission (Sridharan et al., 2002; Beuther et al., 2002d) and X-ray sources (Beuther et al., 2002a), denoting the ongoing formation of intermediate-to-high mass stars. The region is embedded within a cluster of over 800 components detected at NIR wavelengths (Martín-Hernández et al., 2008; Qiu et al., 2008), and it has a rich and energetic outflow component with multiple outflows detected in CO (Beuther et al., 2002c, 2003). Beuther et al. (2002b) found that the large-scale mm emission shows two massive gas clumps roughly aligned in a north-south direction that splits into several subsources with increasing spatial resolution (Beuther & Schilke 2004).

With their studies of the mm continuum at high spatial resolution, Beuther & Schilke (2004) were able to derive the mass function of IRAS 19410+2336, resulting in a Salpeter-like distribution. However, the strongest caveat in the derivation of that mass function was the fact that a uniform dust temperature was used in the calculation of the masses. Although they argue that the dust temperature distribution should not vary strongly, they also warn that changes in the temperature of the cores would result in a somewhat flattened slope.

We have revisited IRAS 19410+2336 observing the mm continuum at high-spatial resolution and obtaining molecular-line emission of known temperature tracers, to determine via several methods a temperature structure for it and in the end derive a more robust mass function.

2. Observations

2.1. Interferometric

We observed the two protostellar clusters of IRAS 19410+2336 with the PdBI in the *B* (Feb-2005), *C* (Dec-2004/Mar-2005) and *D* (Apr-2005) configurations, comprising baselines from 20 m to 330 m. This translates into projected baselines ranging from $\sim 7 k\lambda$ to $\sim 120 k\lambda$ at 3 mm and from $\sim 15 k\lambda$ to $\sim 240 k\lambda$ at 1.4 mm. The phase centers were set at RA(J2000) =

$19^h43^m10.7^s$; Dec(J2000) = $23^\circ44'58.4''$ for the “Northern” (proto)cluster and at RA(J2000) = $19^h43^m11.2^s$; Dec(J2000) = $23^\circ44'03.2''$ for the “Southern” (proto)cluster. The continuum was mapped at 3 mm and 1.4 mm.

Table 1. Observed molecular transitions and rms of the respective maps.

Transition	ν (GHz)	Spectral Resol. (MHz)	E_{up} (K)	rms ^a (mJy beam ⁻¹)	
				North	South
$\text{CH}_3\text{CN}(6_0 - 5_0)$	110.383	0.18	18.5	10	17
$\text{CH}_3\text{CN}(6_1 - 5_1)$	110.381	0.18	25.7	10	17
$\text{CH}_3\text{CN}(6_2 - 5_2)$	110.375	0.18	47.1	10	14
$\text{CH}_3\text{CN}(6_3 - 5_3)$	110.364	0.18	82.9	10	14
$\text{H}_2\text{CO}(3_{0,3} - 2_{0,2})^b$	218.222	0.36	21.0	29	36
$\text{H}_2\text{CO}(3_{2,2} - 2_{2,1})^b$	218.476	0.36	68.1	19	30
$\text{H}_2\text{CO}(3_{2,1} - 2_{2,0})$	218.760	0.36	68.1	23	34

Notes. ^(a) For a spectral resolution of 0.5 km s^{-1} . ^(b) rms values obtained after combining 30 m and PdBI data.

The 3 mm receiver was tuned in the upper sideband and the 1.4 mm receiver in the lower sideband. With this spectral setup we observed the H_2CO and CH_3CN transitions described in Table 1 with a maximum spectral resolution of 0.5 km s^{-1} , adopting a systemic velocity $V_{\text{LSR}} = 22.4 \text{ km s}^{-1}$ (Ridge & Moore, 2001; Tieftrunk et al., 1998).

The phase and amplitude calibrators were 1923+210 and 2023+336 and the flux calibrators were 3C273, 2200+420, 1749+096 and 1741-038, adopting for the calibration the flux values from the SMA flux monitoring of these quasars¹. The data were calibrated with CLIC and then imaged with MAPPING, both part of the GILDAS package². The spectra were processed with CLASS90, also from the GILDAS package.

After imaging and deconvolution, the resulting synthesized beams for the continuum data are $1.2'' \times 0.8''$ at 1.4 mm and $2.2'' \times 1.6''$ at 3 mm. At the given distance of 2.2 kpc that means a spatial resolution of ~ 2200 and ~ 4200 AU, respectively. The continuum data for the Northern (proto)cluster have rms noise levels $\sigma \sim 0.8 \text{ mJy beam}^{-1}$ and $\sigma \sim 0.4 \text{ mJy beam}^{-1}$ at 1.4 mm and 3 mm respectively, while in the southern (proto)cluster the rms noise levels are $\sigma \sim 1.0 \text{ mJy beam}^{-1}$ and $\sigma \sim 0.4 \text{ mJy beam}^{-1}$ at 1.4 mm and 3 mm respectively. For the line data, the synthesized beams and noise levels are detailed in Table 1.

2.2. Short spacings

We obtained IRAM 30 m observations of $\text{H}_2\text{CO}(3_{0,3} - 2_{0,2})$ and $\text{H}_2\text{CO}(3_{2,2} - 2_{2,1})$ towards IRAS 19410+2336 in November 2007, taken in the on-the-fly mode with both HERA heterodyne receivers tuned at 218.222 GHz. For the backend we used the VESPA correlator, assigning 2 of its spectral bands to each HERA receiver, with a channel spacing of 320 kHz and a bandwidth of 80 MHz, resulting in a spectral resolution of 0.5 km/s at 218 GHz.

The data were processed with CLASS90. The single-dish uv-data were combined with the interferometric uv-data using

¹ <http://sma1.sma.hawaii.edu/callist/callist.html>

² <http://www.iram.fr/IRAMFR/GILDAS>

MAPPING. After imaging and deconvolution we obtained a synthesized beam of $1.6'' \times 1.0''$ for the combined data. The rms levels of the combined data are shown in Table 1.

3. Results

3.1. Millimetric Continuum

We established a detection threshold of 4σ in our 1.4 mm continuum maps, corresponding to $\sim 4 \text{ mJy beam}^{-1}$, $M \sim 1 M_{\odot}$ and $N(\text{H}_2) \sim 6 \times 10^{23} \text{ cm}^{-2}$ in the Southern (proto)cluster, and $\sim 3.2 \text{ mJy beam}^{-1}$, $M \sim 0.8 M_{\odot}$ and $N(\text{H}_2) \sim 4.5 \times 10^{23} \text{ cm}^{-2}$ in the Northern (proto)cluster. In the latter we detect 7 sources, while in the former there are 19 sources detected. Figure 1 shows the 1.4 mm and 3 mm continuum maps for both (proto)clusters, with the 26 sources detected at 1.4 mm marked with triangles and the two sources only detected at 3 mm marked with squares.

The properties of the sources are summarized in Table 2. Columns 2 and 3 give their absolute positions, the measured peak flux intensity and integrated flux density are given in columns 4 and 5 respectively. For the unresolved sources, their angular size is typically less than the synthesized beam at the respective wavelength.

Because the brightness temperature at 1.4 mm of the corresponding Planck function for the strongest source in the region is about 2 K, just $\sim 2\%$ of the typical hot core temperatures of ~ 100 K, we can assume that the emission comes from optically thin dust and thus calculate the masses and column densities with the approach outlined by Hildebrand (1983) and adapted by Beuther et al. (2002b, 2005). We adopted a distance of 2.2 kpc, and used a grain emissivity index $\beta = 2$, corresponding to a dust opacity per unit mass $\kappa_{1.4 \text{ mm}} \sim 0.3$ and $\kappa_{3 \text{ mm}} \sim 0.08 \text{ cm}^2 \text{ g}^{-1}$ for a median grain size $a = 0.1 \mu\text{m}$, a grain mass density $\rho = 3 \text{ g cm}^{-3}$, and a gas-to-dust ratio of 186 (Draine et al., 2007).

The selected value of $\beta = 2$ for the grain emissivity index is the value assumed by Beuther & Schilke (2004, see also Beuther et al. 2005), and is the typical value found for the ISM dust (e.g., Hildebrand 1983; Ossenkopf & Henning 1994; Rodmann et al. 2006). Generally, β is thought to range from 1 to 2. When an IR-to-mm SED is available, as is the case now with *Herschel* results, authors have found β values in that range and even higher. Examples are $\beta \sim 1.2$ and 1.5 in Rathborne et al. (2008), or $\beta \sim 1.7 - 3.3$ in Anderson et al. (2010) and $\beta \sim 1.0 - 1.8$ in Rodón et al. (2010). For IRAS 19410+2336, there is no data available to directly calculate the dust opacity index. Therefore, in this work we adopted $\beta = 2$.

In contrast to the bolometer observations of the single dish data (see below), the interferometric continuum data are produced from the line-free part of the spectrum, therefore line contribution to the emission is negligible. Potential contribution from free-free emission is insignificant as well, since the flux at cm wavelengths is on the 1 mJy level and only for the central source in the south, with no emission detected from the other sources (Beuther et al., 2003). Therefore, we can safely assume that the mm continuum from which the masses are calculated is not severely contaminated by free-free emission.

The calculated masses and H_2 column densities are in columns 7 and 8 of Table 2, respectively. For their calculation we assumed the temperatures shown in column 11 of Table 3. Those temperatures were determined from the measured H_2CO line ratios, following the procedure explained and discussed in Section 4.2. The visual extinctions in column 9 were calculated assuming $A_v = N(\text{H}_2)/0.94 \times 10^{21}$ (Frerking et al., 1982).

³ For $T_k \sim 40$ K (see Secs. 3.1 and 4.1.2 for more details).

The masses obtained are strongly affected by the spatial filtering inherent to interferometers. While varying dust properties may account for some of the discrepancy between the masses calculated at 1.4 mm and 3 mm, the spatial filtering is most likely the main cause. Comparison with single-dish continuum observations of IRAS 19410+2336 at 1.2 mm with the IRAM 30m Telescope (Beuther et al., 2002b) show that in our 1.4 mm continuum map of the southern (proto)cluster we are recovering only $\sim 6\%$ of the flux estimated with single dish observations. On the other hand, at 3 mm we recover a relatively larger amount of the single dish flux, $\sim 37\%$. This shows that there is a large fraction of the mass contained in extended structures, that we are filtering out.

The different percentage of flux filtered out in each wavelength band can be explained in the same way as the large (up to a factor ~ 10) difference between the calculated masses at 1.4 mm and 3 mm. Both wavelengths were observed at the same time with the same interferometer configurations meaning that although the ground baselines are the same, the uv coverage measured in units of wavelength ($k\lambda$) at 3 mm is more compact than at 1.4 mm, therefore tracing more extended components in the region.

In the following, we assume that the missing flux is smoothly distributed and affects all cores in the same way. This assumption comprises one important caveat when deriving a CMF at high-spatial resolution, described in more detail in section 5.4.

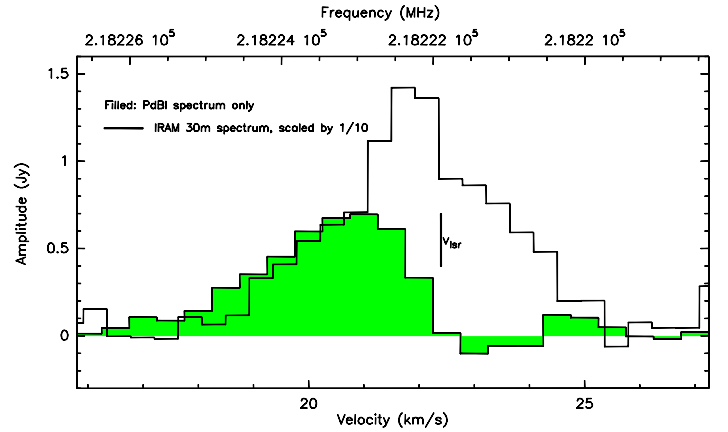


Fig. 2. Comparison of the interferometer (PdBI, filled) and single-dish (IRAM 30m, solid line) $\text{H}_2\text{CO}(3_{0,3} - 2_{0,2})$ line emission towards IRAS 19410+2336. Clearly seen is the “self-absorption”-like feature in the PdBI emission, denoting the missing flux coming from more extended spatial-scales and filtered out by the interferometer. The single-dish spectrum has been scaled down for comparison by a factor 10.

3.2. Formaldehyde

With the purpose of estimating the temperature structure of IRAS 19410+2336, we observed three H_2CO transitions known to be usable as a gas thermometer (e.g., Mangum & Wootten 1993, see Sec. 4.2).

Since the PdBI data are clearly affected by missing short spacings (an example of this is shown in Figure 2), the region was also observed with the IRAM 30m telescope. Figure 3 shows the integrated intensity maps of the combined PdBI+IRAM 30m data.

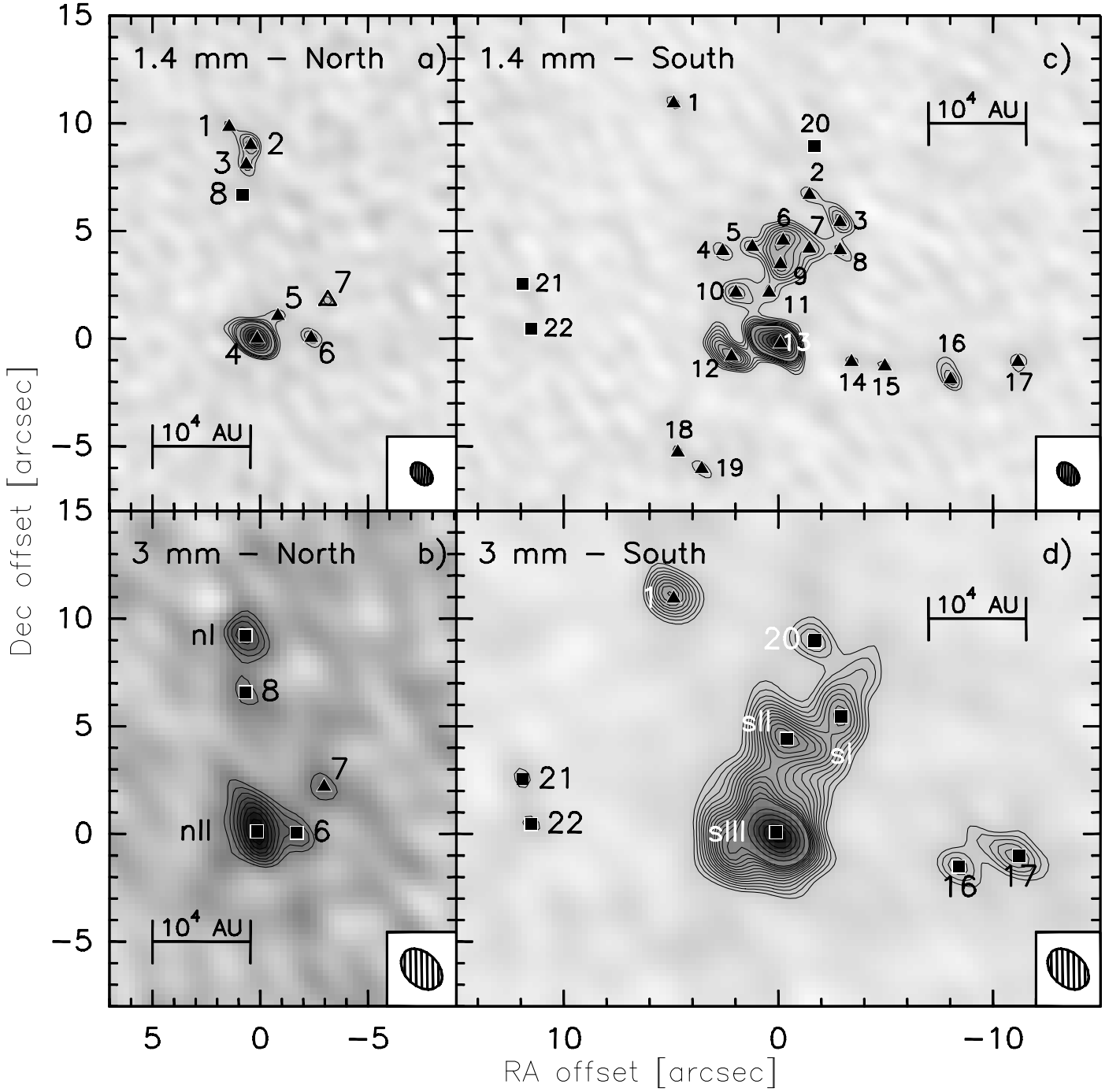


Fig. 1. Continuum maps of IRAS 19410+2336 obtained with the PdBI. In the top row are the 1.4 mm maps of the Northern (panel *a*) and Southern (panel *c*) (proto)clusters. Similarly, in the bottom row are the 3 mm maps of the Northern and Southern (proto)clusters in panels *b* and *d* respectively. The contouring starts at the 4σ level in all the panels. Contours in panel *a* increase in 1σ steps up to 8σ and in 4σ steps afterwards, in panel *b* in 4σ steps, in panel *c* in 1σ steps up to 11σ and in 4σ steps afterwards, and in panel *d* in 1σ steps up to 16σ and in 4σ steps afterwards. See Table 2 for the σ values. The triangles mark the position of the sources detected at 1.4 mm while the squares are the sources detected at 3 mm. A square appearing in a 1.4 mm map indicates a source that is only detected at 3 mm. Similarly, a triangle in a 3 mm map signals a source detected at the same position in a 1.4 mm map.

Of the three detected H_2CO lines, $\text{H}_2\text{CO}(3_{0,3} - 2_{0,2})$ and $\text{H}_2\text{CO}(3_{2,2} - 2_{2,1})$ are the ones with the best signal-to-noise ratio. According to Mangum & Wootten (1993) those two transitions are enough to determine temperatures, therefore we did not use the third detected transition, $\text{H}_2\text{CO}(3_{2,1} - 2_{2,0})$, for the temperature analysis.

Both $\text{H}_2\text{CO}(3_{0,3} - 2_{0,2})$ and $\text{H}_2\text{CO}(3_{2,2} - 2_{2,1})$ have their strongest emission peak towards the brightest mm source detected in the continuum in both the north and south (proto)clusters. The secondary peaks in all the maps are in the same spatial region as the continuum emission, however there is no spatial correlation between the secondary peaks in the H_2CO

Table 2. Properties of the continuum mm sources in IRAS 19410+2336.

Source	R.A. (J2000)	Dec. (J2000)	I_ν (mJy beam ⁻¹)	S_ν (mJy)	T_k^a (K)	Mass (M_\odot)	$N(H_2)$ (10^{23} cm^{-2})	A_ν (10^3 mag)	Flags
1.4 mm with a $1.2'' \times 0.8''$ beam									
1-s ...	19 43 11.553	23 44 14.15	4.8	...	35	1.5	8.2	0.9	<i>u</i>
2-s ...	19 43 11.093	23 44 09.90	5.7	...	35	1.7	9.6	1.0	<i>u</i>
3-s ...	19 43 10.989	23 44 08.64	8.1	8.3	35	2.5	14	1.5	
4-s ...	19 43 11.387	23 44 07.29	5.3	...	35	1.6	9.0	1.0	<i>u</i>
5-s ...	19 43 11.286	23 44 07.49	6.2	...	35	1.9	10	1.1	<i>u</i>
6-s ...	19 43 11.182	23 44 07.78	1.1	16	35	4.9	19	2.0	
7-s ...	19 43 11.093	23 44 07.41	7.6	7.7	35	2.4	13	1.4	
8-s ...	19 43 10.989	23 44 07.33	5.6	...	35	1.7	9.4	1.0	<i>u</i>
9-s ...	19 43 11.191	23 44 06.68	1.0	14	35	4.3	17	1.8	
10-s ...	19 43 11.342	23 44 05.37	7.2	11	35	3.4	12	1.3	
11-s ...	19 43 11.229	23 44 05.37	5.6	...	35	1.7	9.5	1.0	<i>u</i>
12-s ...	19 43 11.357	23 44 02.39	1.3	24	45	5.5	17	1.8	
13-s ...	19 43 11.191	23 44 03.00	4.2	75	90	8.1	25	2.7	
14-s ...	19 43 10.950	23 44 02.15	4.6	...	35	1.4	7.8	0.8	<i>u</i>
15-s ...	19 43 10.837	23 44 01.94	4.8	...	35	1.5	8.1	0.9	<i>u</i>
16-s ...	19 43 10.614	23 44 01.33	7.3	...	35	2.2	13	1.4	<i>u</i>
17-s ...	19 43 10.385	23 44 02.15	5.1	...	35	1.6	8.7	1.0	<i>u</i>
18-s ...	19 43 11.539	23 43 57.94	4.6	...	35	1.4	7.8	0.8	<i>u</i>
19-s ...	19 43 11.458	23 44 57.17	5.3	...	35	1.6	9.0	1.0	<i>u</i>
1-n ...	19 43 10.801	23 45 08.26	3.4	...	35	1.0	5.8	0.6	<i>u</i>
2-n ...	19 43 10.728	23 45 07.41	6.1	...	35	1.9	11	1.0	<i>u</i>
3-n ...	19 43 10.743	23 45 06.51	4.5	...	35	1.4	7.6	0.8	<i>u</i>
4-n ...	19 43 10.706	23 44 58.42	2.7	32	60	5.3	25	2.7	
5-n ...	19 43 10.636	23 44 59.48	3.6	...	50	0.7	4.1	0.4	<i>u</i>
6-n ...	19 43 10.524	23 44 58.45	4.7	...	35	1.4	7.9	0.8	<i>u</i>
7-n ...	19 43 10.469	23 45 00.2	3.6	...	35	1.1	6.1	0.6	<i>u</i>
3 mm with a $2.2'' \times 1.6''$ beam									
1-s ...	19 43 11.558	23 44 14.41	5.1	...	40	19.9	32	3.4	<i>u</i>
20-s ...	19 43 11.073	23 44 12.23	3.1	...	40	12.1	19	2.1	<i>u, n</i>
c3mm-sI ...	19 43 10.986	23 44 08.67	4.8	6.7	40	26.2	29	3.1	c(2,3,8-s)
c3mm-sII ...	19 43 11.170	23 44 07.64	6.6	13	40	50.8	40	4.2	c(5,6,7,9-s)
c3mm-sIII ...	19 43 11.206	23 44 03.29	17.7	48	40	187.5	102	10.8	c(10,11,12,13-s)
16-s ...	19 43 10.587	23 44 01.71	2.9	...	40	11.2	18	1.9	<i>u</i>
17-s ...	19 43 10.382	23 44 02.20	3.5	3.9	40	15.2	22	2.3	
21-s ...	19 43 12.066	23 44 05.76	2.0	...	40	7.9	12	1.3	<i>u, n</i>
22-s ...	19 43 12.037	23 44 03.68	2.0	...	40	7.7	12	1.3	<i>u, n</i>
c3mm-nI ...	19 43 10.746	23 45 07.63	3.2	...	40	12.7	20	2.1	<i>u, c(1,2,3-n)</i>
8-n ...	19 43 10.746	23 45 05.01	1.9	...	40	7.5	12	1.2	<i>u, n</i>
c3mm-nII ...	19 43 10.707	23 44 58.54	5.1	7.4	40	29.0	31	3.3	c(4,5-n)
6-n ...	19 43 10.573	23 44 58.47	2.6	...	40	10.2	16	1.7	<i>u</i>
7-n ...	19 43 10.480	23 45 00.61	2.2	...	40	8.5	13	1.4	<i>u</i>

Notes. The last column indicates unresolved cores (*u*) and detections at 3 mm without a 1.4 mm counterpart (*n*). The c(X,Y,Z) flag indicates that the source is the unresolved combination of sources X, Y and Z. If the source is unresolved, its mass in Column 7 is calculated with the peak intensity value of Column 4.

^(a) Derived from the H₂CO emission, the 3 mm temperatures are the average in the region (see Sec. 4.1.2). The values for the 1.4 mm cores are the same as in Table 3, and are repeated here just for reading convenience.

and dust emission. This prevents us to obtain a temperature for each individual core.

There is an emission feature seen in the northern cluster in both H₂CO ($3_{0,3} - 2_{0,2}$) and H₂CO ($3_{2,2} - 2_{2,1}$) transitions $\sim 4''$ southeast of the main peak, marked with a star in the upper panels of Figure 3. The feature is at the rest velocity, and we do not

detect continuum emission neither at 1.4 mm nor at 3 mm at that position.

The first-moment maps of the combined PdBI+30m data (see Fig. 4) show only a small velocity dispersion of $\sim 1 \text{ km s}^{-1}$ in both (proto)clusters for the observed H₂CO lines. Similarly,

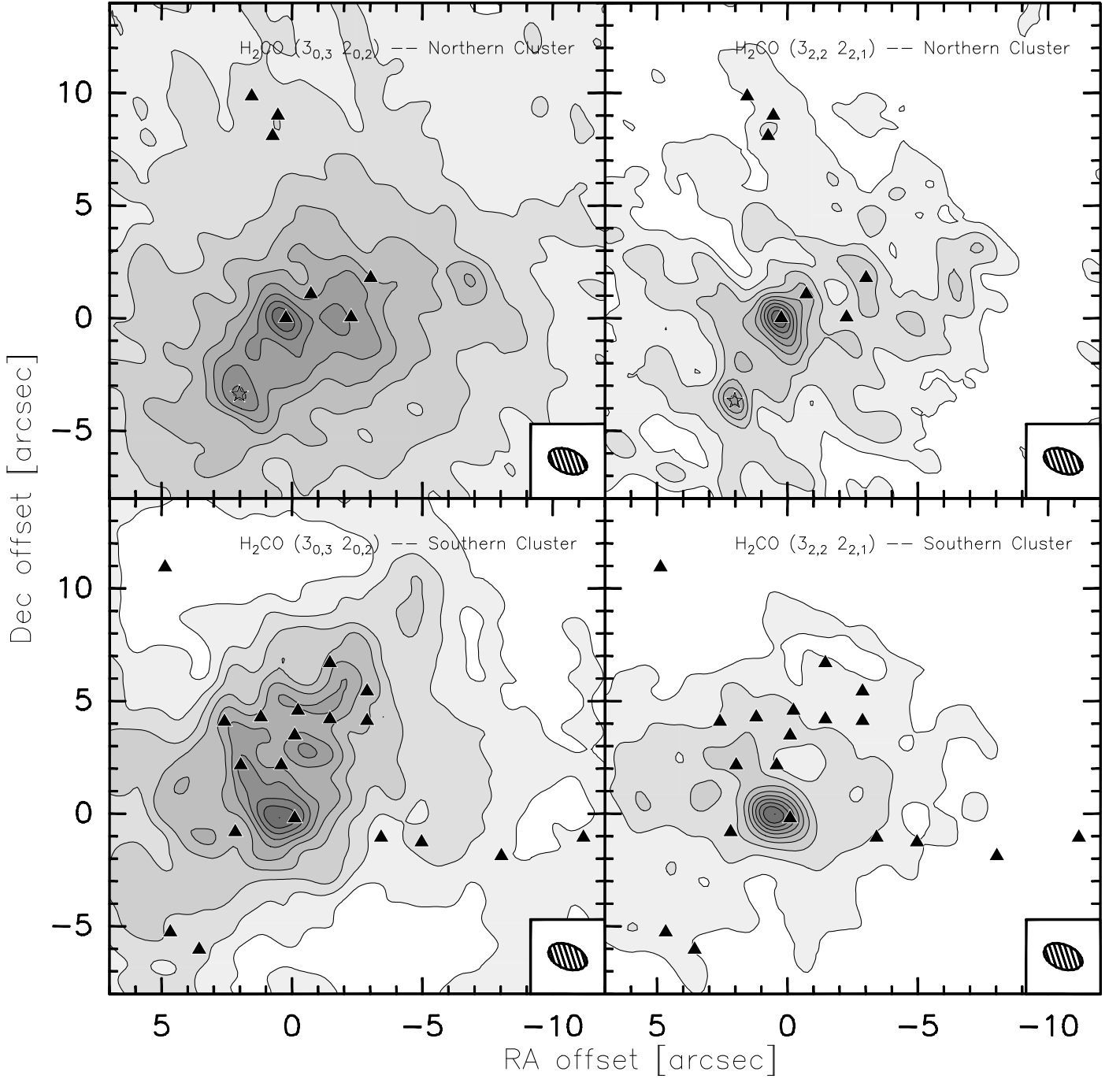


Fig. 3. Combined PdBI and IRAM30m integrated emission of H_2CO towards IRAS 19410+2336. In the left panels are the $\text{H}_2\text{CO}(3_{0,3} - 2_{0,2})$ transition in the Northern (upper panel) and Southern (lower panel) (proto)clusters, and in the right panels of the image are the $\text{H}_2\text{CO}(3_{2,2} - 2_{2,1})$ transition. The contour levels are in 10% steps of the peak integrated intensity for each map. The triangles mark the 1.4 mm sources detected, and the $1.6'' \times 1''$ beam appears in the lower-right corner of each panel.

the second-moment maps show no strong variation over the (proto)clusters.

3.3. Methyl Cyanide

We observed the $K = 0 - 3$ components of the $\text{CH}_3\text{CN}(6_K - 5_K)$ ladder, which are a useful thermometer for the dense gas (e.g., Loren & Mundy 1984; Zhang et al. 1998). We detected CH_3CN emission only towards sources 13-s, 6/7/9-s and 4-n. Figure 5 shows the CH_3CN spectra toward those three positions.

The $K=0$ and $K=1$ components were detected at the three positions, and towards 13-s we also detect the $K=2$ and $K=3$ components. Since that is the only position at which those transitions are seen, this implies that 13-s is the warmest in the region. Also there is a tentative detection of the $K=2$ component towards 4-n.

Unlike with the H_2CO transitions, CH_3CN is a dense gas tracer, and it is barely affected by the missing short-spacings.

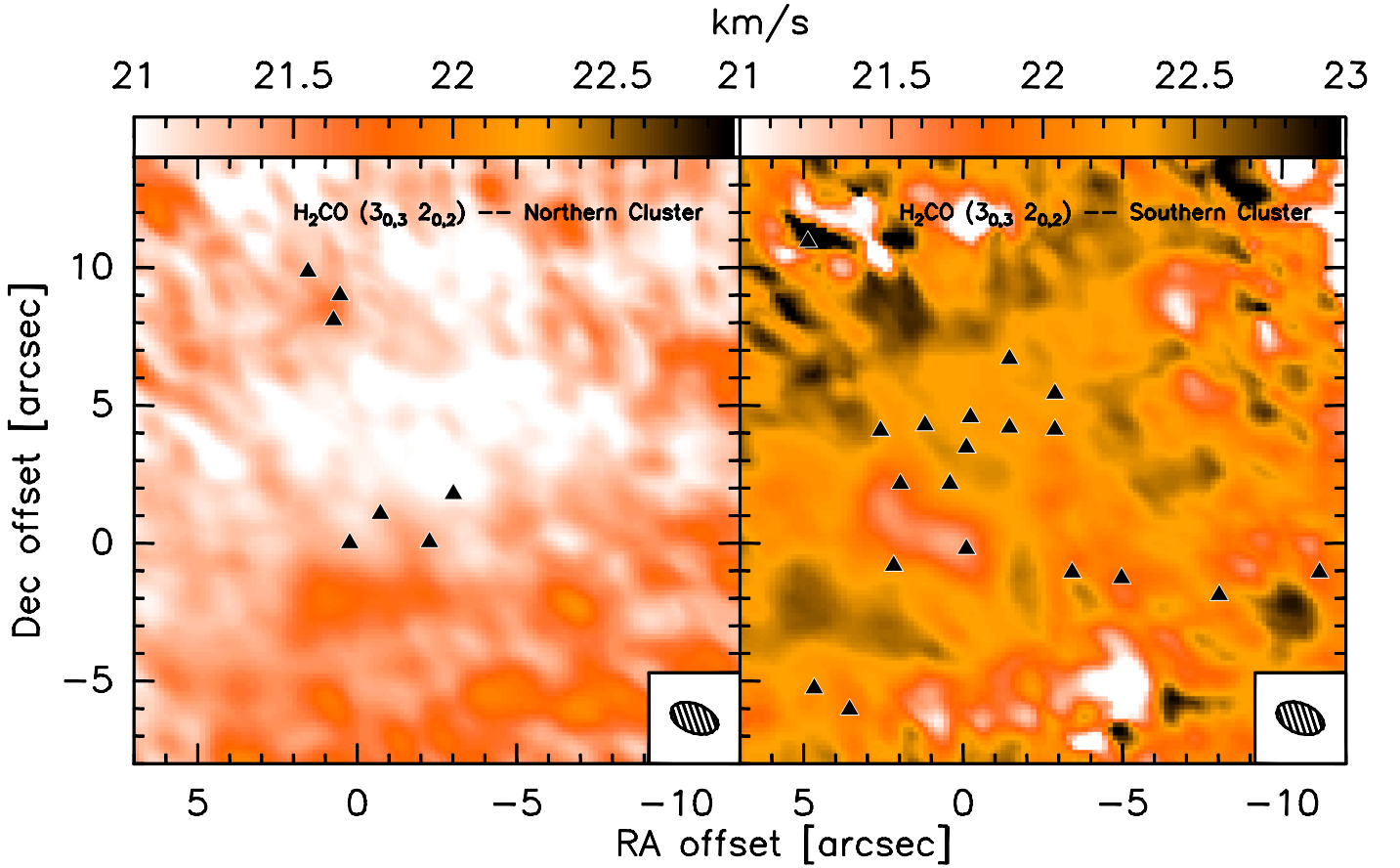


Fig. 4. Combined PdBI and IRAM 30m first moment maps of $\text{H}_2\text{CO} (3_{0,3} - 2_{0,2})$ towards IRAS 19410+2336 for the Northern (left panel) and Southern (right panel) (proto)clusters. The triangles mark the continuum sources detected, and the beam appears in the lower-right corner of each panel. There is no signature of a strong velocity dispersion.

4. Deriving the Core Mass Function

4.1. Temperature determination

One of the major caveats of Beuther & Schilke (2004) in deriving a CMF for IRAS 19410+2336 was the assumption of a uniform temperature for both north and south (proto)clusters when deriving the masses of the cores. In this work, we try to derive a temperature structure for the two subclusters to obtain more accurate core masses and by that a more reliable CMF.

In this section we describe the process used to determine the temperature of the detected cores. However it has to be taken into account that we are assuming that the kinetic temperatures derived from combined PdBI+30m molecular-line analysis correspond to the dust temperatures of PdBI continuum peaks. As is further discussed in Sec. 5.4 this is not ideal, but is one of the limitations that we still have to face when working with high-spatial resolution mm observations. While combining single-dish and interferometer line data is relatively easy, the vastly different continuum bandpasses of interferometers and single-dish bolometers make the combination of continuum data extremely difficult.

4.1.1. Applying H_2CO line ratios

Formaldehyde (H_2CO), one of the first polyatomic molecules discovered in space, has proven its usefulness to derive physical properties of the interstellar gas (e.g., Mangum & Wootten 1993; Jansen et al. 1994, 1995;

Mühle et al. 2007; Watanabe & Mitchell 2008). In particular, H_2CO allows one to estimate the kinetic temperature and the spatial density in star-forming regions.

Because H_2CO is almost a symmetric rotor ($\kappa = -0.96$), transitions between energy levels with different K are only collisionally excited. Therefore the comparison between the level populations from different K components from the same $\Delta J = 1$ transition gives a measure of the kinetic temperature of the medium (Mangum & Wootten, 1993).

In this work, we used the line intensity ratios of the $\text{H}_2\text{CO} (3_{0,3} - 2_{0,2})$ and $\text{H}_2\text{CO} (3_{2,2} - 2_{2,1})$ transitions, with energies $E_{up} \sim 21$ K and $E_{up} \sim 68$ K, respectively. These transitions meet the criteria previously mentioned and are only ~ 254 MHz apart, therefore they could be observed within the same spectral setup of the PdBI receivers and the HERA heterodyne receiver. In this way, possible instrumental uncertainties such as telescope efficiency as a function of wavelength, or receiver and pointing instabilities, can be disregarded. Hence, one can obtain line ratios that are not affected by instrumental effects.

Since there is only a poor spatial correlation between the combined H_2CO and continuum emission, we cannot extract a temperature for each individual core but only a temperature structure of the (proto)clusters as a whole. Only for the brightest continuum cores it was possible to associate the H_2CO and dust emission. Their spectra are shown in Figure 6.

Having this temperature information is already an improvement than just assuming a single temperature for all cores.

Table 3. H₂CO line parameters for the detected cores.

Source	H ₂ CO (3 _{0,3} – 2 _{0,2})				H ₂ CO (3 _{2,2} – 2 _{2,1})				Ratio	T _k ^c (K)
	T _b (K)	∫ T _b dv (K km s ⁻¹)	v _c (km s ⁻¹)	Width (km s ⁻¹)	T _b (K)	∫ T _b dv (K km s ⁻¹)	v _c (km s ⁻¹)	Width (km s ⁻¹)		
1-s ^a	0.4 ± 0.2	1 ± 0.4	20.4 ± 0.6	2.7 ± 1.2	...	35
2-s	14.7 ± 0.5	45.7 ± 0.8	22.2 ± 0.1	3.0 ± 0.1	1.7 ± 0.3	4.5 ± 0.8	21.7 ± 0.2	2.5 ± 0.6	8.5	35
3-s	13.6 ± 0.5	40.8 ± 0.9	22.3 ± 0.1	2.8 ± 0.1	1.9 ± 0.4	3.5 ± 0.4	21.3 ± 0.1	1.7 ± 0.3	7.0	35
4-s	17.1 ± 0.8	51.8 ± 0.8	22.3 ± 0.1	2.8 ± 0.1	3.0 ± 0.3	7.4 ± 0.7	21.9 ± 0.1	2.3 ± 0.3	5.8	35
5-s	17.5 ± 0.7	54.4 ± 0.8	22.3 ± 0.1	2.9 ± 0.1	2.7 ± 0.2	7.4 ± 0.8	21.5 ± 0.1	2.6 ± 0.4	6.5	35
6-s	18.0 ± 0.9	56.3 ± 1.1	22.2 ± 0.1	2.9 ± 0.1	1.8 ± 0.4	6.8 ± 0.8	21.4 ± 0.2	3.5 ± 0.6	9.8	35
7-s	18.1 ± 0.7	54.6 ± 0.8	22.2 ± 0.1	2.8 ± 0.1	2.3 ± 0.2	5.9 ± 0.8	21.0 ± 0.2	2.4 ± 0.4	7.8	35
8-s	12.4 ± 0.4	39.0 ± 0.9	22.3 ± 0.1	3.0 ± 0.1	1.8 ± 0.3	4.1 ± 0.4	20.9 ± 0.1	2.2 ± 0.2	7.0	35
9-s	20.5 ± 1.1	62.7 ± 0.6	22.2 ± 0.1	2.9 ± 0.1	2.6 ± 0.5	7.3 ± 0.5	21.6 ± 0.1	2.6 ± 0.2	7.7	35
10-s	18.4 ± 1.3	61.2 ± 1.3	22.3 ± 0.1	3.1 ± 0.1	2.7 ± 0.4	9.3 ± 1.2	21.5 ± 0.2	3.2 ± 0.5	6.8	35
11-s	19.2 ± 0.7	58.3 ± 1.0	22.1 ± 0.1	2.8 ± 0.1	3.0 ± 0.5	8.4 ± 0.9	21.3 ± 0.1	2.6 ± 0.3	6.5	35
12-s	12.8 ± 0.6	38.7 ± 0.6	22.1 ± 0.1	2.8 ± 0.1	2.6 ± 0.4	8.0 ± 1.1	21.3 ± 0.2	2.9 ± 0.5	4.9	45
13-s	14.9 ± 1.0	83.5 ± 0.8	21.6 ± 0.1	3.8 ± 0.1	4.8 ± 0.5	21.7 ± 0.8	20.8 ± 0.1	3.0 ± 0.1	3.1	90
14-s	5.8 ± 0.2	13.3 ± 0.7	22.1 ± 0.1	2.1 ± 0.1	1.7 ± 0.5	5.1 ± 0.8	21.2 ± 0.2	2.9 ± 0.6	3.5	35
15-s	6.5 ± 0.7	21.6 ± 1.1	22.3 ± 0.1	3.1 ± 0.2	1.8 ± 0.1	...	21.4 ± 0.1	unresolved	3.6	35
16-s	3.5 ± 0.2	8.6 ± 0.8	22.2 ± 0.1	2.3 ± 0.3	0.8 ± 0.1	...	21.3 ± 0.2	unresolved	4.2	35
17-s	4.1 ± 0.3	10.8 ± 0.7	22.4 ± 0.1	2.5 ± 0.2	1.8 ± 0.1	...	22.2 ± 0.1	unresolved	2.3	35
18-s	8.4 ± 0.7	25.3 ± 0.9	22.4 ± 0.1	2.8 ± 0.1	3.1 ± 0.1	...	21.5 ± 0.1	unresolved	2.7	35
19-s	8.0 ± 0.6	21.6 ± 0.8	22.4 ± 0.1	2.5 ± 0.1	1.0 ± 0.3	3.1 ± 0.5	22.0 ± 0.3	2.8 ± 0.5	7.9	35
1-n	0.8 ± 0.3	3.3 ± 0.7	21.3 ± 0.5	4.0 ± 1.1	0.2 ± 0.1	2.3 ± 0.9	23.9 ± 1.8	9.3 ± 3.5	3.4	35
2-n	1.4 ± 0.2	4.2 ± 0.6	21.1 ± 0.2	3.0 ± 0.6	0.8 ± 0.1	1.3 ± 0.6	20.7 ± 0.3	1.6 ± 1.1	1.7	35
3-n	1.4 ± 0.1	5.1 ± 0.7	21.3 ± 0.2	3.4 ± 0.6	0.5 ± 0.3	2.5 ± 0.9	22.8 ± 0.9	4.9 ± 2.1	2.9	35
4-n	7.8 ± 0.7	35.6 ± 1.1	21.0 ± 0.1	4.3 ± 0.2	2.7 ± 0.4	12.2 ± 1.2	20.5 ± 0.2	4.2 ± 0.5	2.9	60
5-n	5.4 ± 0.2	13.6 ± 0.9	21.2 ± 0.1	2.4 ± 0.2	1.8 ± 0.3	6.0 ± 1.0	20.2 ± 0.2	3.2 ± 0.7	3.0	50
6-n	6.8 ± 0.2	20.2 ± 0.9	21.3 ± 0.1	2.8 ± 0.1	1.4 ± 0.1	3.4 ± 0.8	20.7 ± 0.3	2.3 ± 0.7	4.9	35
7-n	5.6 ± 0.7	16.4 ± 1.3	20.6 ± 0.1	2.7 ± 0.3	1.4 ± 0.3	5.9 ± 0.7	20.5 ± 0.2	4.1 ± 0.6	4.2	35

Notes. ^(a) No detection in H₂CO (3_{0,3} – 2_{0,2}) ^(b) Obtained with a 3'' beam to avoid the optically thick regime. ^(c) From the LVG analysis in section 4.1.2

4.1.2. LVG modeling

We extracted spectra towards the positions of each of the 26 sources detected at 1.4 mm and processed them with CLASS90, the obtained line parameters are listed in Table 3. Once we obtained the $R = \text{H}_2\text{CO}(3_{0,3} - 2_{0,2})/\text{H}_2\text{CO}(3_{2,2} - 2_{2,1})$ line ratios, they were compared with LVG model predictions of the behavior of R as a function of molecular hydrogen density $n(\text{H}_2)$, formaldehyde column density $N(\text{H}_2\text{CO})$, and kinetic temperature T_k .

The H₂ density could be estimated from our data. With the continuum emission measured towards the positions of the different sources, we estimate a beam-averaged H₂ column density $N(\text{H}_2)$ ranging from $\sim 5 \times 10^{23} \text{ cm}^{-2}$ to $\sim 6 \times 10^{24} \text{ cm}^{-2}$ with a mean value of $\sim 10^{24} \text{ cm}^{-2}$. For this calculation we assumed a priori a uniform temperature $T_k = 46 \text{ K}$ (Beuther & Schilke, 2004).

Considering spherical symmetry for the (proto)clusters, at the given distance of 2.2 kpc and if θ is the angular diameter of the (proto)cluster, the relationship

$$n(\text{H}_2) = 1.5 \times 10^{-16} \text{ cm}^{-3} \left[\frac{N(\text{H}_2)}{\text{cm}^{-2}} \right] \left[\frac{\text{kpc}}{d} \right] \left[\frac{\text{arcsec}}{\theta} \right] \quad (1)$$

gives an average value $n(\text{H}_2) \sim 10^7 \text{ cm}^{-3}$ for each (proto)cluster. For the calculation we adopted an approximate size of $\theta \sim 9''$ for

the protoclusters, considering the extension of the main 1.4 mm emission. This translates to a size of $\sim 20000 \text{ AU}$ at 2.2 kpc.

In contrast to $n(\text{H}_2)$, we cannot directly measure the value of $N(\text{H}_2\text{CO})$ from our data. Values for the H₂CO abundance relative to H₂ are reported in the range of $X(\text{H}_2\text{CO}) \sim 10^{-9} - 10^{-12}$, for $n(\text{H}_2) \sim 10^{4-6} \text{ cm}^{-3}$ (e.g., Wootten et al. 1978; Mundy et al. 1987; Carey et al. 1998; van der Tak et al. 2000), therefore calculations of an average $N(\text{H}_2\text{CO})$ assuming an $X(\text{H}_2\text{CO})$ value from the literature would introduce a high degree of uncertainty.

To constrain the value of $N(\text{H}_2\text{CO})$ we performed a least-squares minimization of the H₂CO(3_{0,3} – 2_{0,2}) and H₂CO(3_{2,2} – 2_{2,1}) line intensities as a function of $n(\text{H}_2)$ and $N(\text{H}_2\text{CO})$ for 13-s, the strongest source in the region. Assuming $T_k = 100 \text{ K}$ (typical for hot cores), we obtain $N(\text{H}_2\text{CO}) \sim 10^{14.5 \pm 0.1} \text{ cm}^{-2}$ and $n(\text{H}_2) \sim 10^{6.4 \pm 1.0} \text{ cm}^{-3}$, as the best solution. This density agrees to within 1σ with the previously calculated $n(\text{H}_2) \sim 10^7 \text{ cm}^{-3}$, while the column density value can be considered as an upper limit since it was derived for the brightest source, with the highest H₂ column density.

We now compare the LVG model predictions of the behavior of the ratio R as a function of $N(\text{H}_2\text{CO})$ and T_k for $n(\text{H}_2) \sim 10^7 \text{ cm}^{-3}$ with the observed R values. Figure 7 shows the comparison. The dotted black contours are the modeled R values from 1 to 10 by $R = 1$ steps, while the solid red contours are the observed R for sources 3-s, 12-s, 13-s and 19-s (for

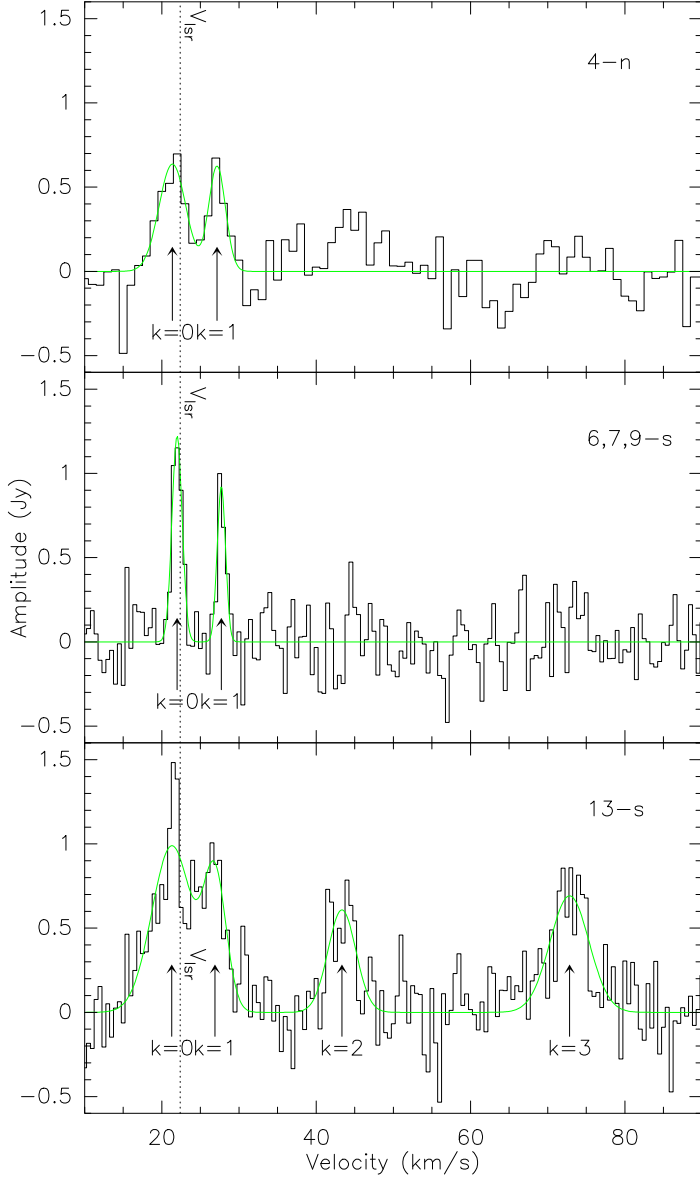


Fig. 5. Observed CH_3CN spectra towards sources 13-s; 6,7,9-s and 4-n. The detected K -components are marked with arrows in each case, and the rest velocity with a dotted line. The green solid line is the best Gaussian fit for the lines, obtained with CLASS, and the resulting line parameters are in Table 4. Only for 13-s were the four K -components detected, indicating a warmer environment.

viewing simplicity, we only plot a few sources here). The vertical gray dotted line mark the previously obtained upper limit value $\log N(\text{H}_2\text{CO}) \sim 14.5$

For $n(\text{H}_2) \sim 10^7 \text{ cm}^{-3}$, the calculated upper limit $N(\text{H}_2\text{CO})$ puts the cores close to the optically thin/thick regime turnover. This turnover is hinted at in the behavior of the contour lines in Figure 7, and is located at $N(\text{H}_2\text{CO}) \sim 10^{15} \text{ cm}^{-2}$. At higher values the temperature is no longer sensitive to the column density, which indicates the onset of the optically thick regime. Another method to (qualitatively) estimate the optical depth is by comparing the kinetic temperature T_k with the brightness temperature T_b . We find that T_b is systematically lower than T_k (see Table 3), therefore if we assume beam-filling the medium is optically thin.

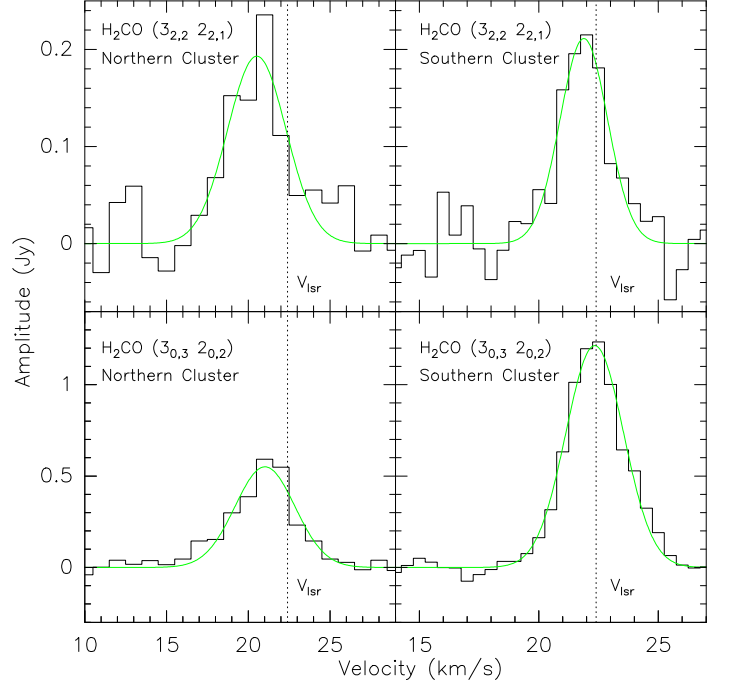


Fig. 6. H_2CO spectra of the main sources in each (proto)cluster of IRAS 19410+2336. In the upper row are the $\text{H}_2\text{CO} (3_{2,2} - 2_{2,1})$ spectra for sources 4-n (left panel) and 13-s (right panel), and similarly in the bottom row are the $\text{H}_2\text{CO} (3_{0,3} - 2_{0,2})$ spectra for those two sources. A Gaussian profile was fit to each spectrum, and is shown by a green solid line. The dotted line marks the rest velocity adopted for the observations.

Near to the turnover, the uncertainty in the temperature becomes larger, and in this case we see that it is approximately $\sim 15 \text{ K}$. To derive this value we considered the uncertainty of $\sigma \sim 0.2 \text{ dex}$ in the derivation of $N(\text{H}_2\text{CO})$. Shifting our upper value for $N(\text{H}_2\text{CO})$ by that amount, the derived temperature varies by $\sim 15 \text{ K}$ for 13-s, the brightest source. This can be seen in Figure 7, where it can also be noticed that this effect is smaller for the sources with lower column density.

As noted before, there is only a poor correlation between the continuum cores and the H_2CO peaks (except for the main sources). Therefore, based on their continuum flux and relative location in the (proto)cluster, we separated the cores into several groups. For each of these groups an average value of T_k was determined based on the values obtained for each of the sources within the group. Column 11 of Table 3 contains the kinetic temperature values assigned to each group which are used to determine the masses and $N(\text{H}_2)$ of the cores shown in Table 2, and to build the mass distribution to fit the CMF.

The majority of cores appear to be relatively cold, with a temperature of $\sim 35 \text{ K}$. Only cores 12-s, 13-s, 4-n and 5-n have higher temperatures, up to $\sim 90 \text{ K}$ in the case of 13-s. This indicates that these cores are harboring a protostar. In the cases of 13-s and 4-n there are reported NIR counterparts (see Sec. 5.2). The average temperature value for the whole region is $\sim 40 \pm 15 \text{ K}$, in agreement with the $T_k \sim 46 \text{ K}$ derived based on IRAS far-infrared observations (Beuther & Schilke, 2004). Consequently, we find that the mean $N(\text{H}_2)$ does not deviate significantly from the value adopted at the beginning despite the changes introduced by the different temperature values (see

Table 2), since that column density was calculated with the IRAS-based temperature.

4.1.3. The CH₃CN k-ladder spectra

Methyl cyanide (CH₃CN) is a dense gas ($n \gtrsim 10^5 \text{ cm}^{-3}$) tracer and can also be used as a temperature determinant. As described previously in Section 3.3 we only detect CH₃CN towards 3 positions, however only for source 13-s we detect enough k -components to derive a temperature, and to that source we apply the analysis described in this section. In the other two cases, we only detect the first two k -components, indicating that those are cold objects.

Two methods were used. First we compared the CH₃CN spectra with LTE model spectra produced with XCLASS (Schilke et al., 1999), a superset of CLASS of the GILDAS package, obtaining a temperature of $\sim 80 \pm 40 \text{ K}$ for 13-s (see Fig. 8). Second, we also derive a rotational diagram to derive the gas temperature (see e.g., Loren & Mundy 1984; Zhang et al. 1998).

For the rotational diagram, we followed the method outlined in Appendix B of Zhang et al. (1998). Basically, we assume LTE and optically thin emission, then the level populations become directly proportional to the line intensities of the k -components and are translated into a single temperature via the Boltzmann equation. With these assumptions, we have the following equation (adapted from eq. [B6] of Zhang et al. 1998) for the relation between the level populations $N_{J,K}$ and the gas temperature T_{rot}

$$\ln \frac{N_{J,K}}{g_{J,K}} \propto -\frac{E_{J,K}}{k} \frac{1}{T_{\text{rot}}} \quad (2)$$

where $g_{J,K}$ and k are the statistical weight of the (J, K) level and the boltzmann constant, respectively. Studies by Wilner et al. (1994) show that T_{rot} derived with this formulation agrees with those obtained with LVG calculations.

The level population for the upper k -level can be obtained from the integrated intensity of the corresponding line. The line parameters obtained from the Gaussian fit of the spectra shown in Figure 5, and the calculated $N_{J,K}$ for each level are in Table 4. The resulting rotational diagram is shown in Figure 9, along with the least-squares fit of all the k -components using eq. (2), obtaining the value $T_{\text{rot}} \sim 100 \pm 60 \text{ K}$ for 13-s.

From the plot it can be seen that the fit does not represent the physical picture well. Explanations of this may be that the assumption of optically thin emission is not correct, therefore the model applied is not right, or that we are mapping a hot and small core with a colder extended envelope, thus presenting two different temperature regimes.

Despite the crude fit, this value agrees very well with the T_k obtained from the H₂CO LVG model and also with the value obtained from the XCLASS model.

4.2. The Differential Core Mass Function

Combining the data from both (proto)clusters we derive a differential CMF $\Delta N/\Delta M$, with the number of cores ΔN per mass bin ΔM .

One of the strongest caveats (see Sec. 5.4) we faced when deriving the CMF was the relatively low number of cores detected. Because of that, a continuous linear binning in mass was not possible. Instead, we performed a logarithmic binning to bet-

ter represent and analyze the data, meaning that the fixed-width mass bins are defined on a logarithmic axis,

$$\Delta M = \log M_k - \log M_{k-1} = B \quad (3)$$

where B is the constant bin width. Therefore, the k -th mass is defined as $M_k = 10^{kB}$. This binning scheme is further discussed in Maíz Apellániz & Úbeda (2005).

A priori we do not have a preferred value for B , thus we derive a mass spectrum for different bin widths, with B ranging from 0.001 to 1 in 0.001 steps. Not all the CMFs obtained with this method were fitted. To obtain meaningful results, we established the following criteria to be satisfied for a CMF to be fitted:

- At most only one bin may contain a single core.
- There must be at least four non-empty bins after the incompleteness threshold.

We fit a power-law of the form $\Delta N/\Delta M \propto M^\beta$ to the CMFs satisfying those two criteria, obtaining a β_B index value corresponding to a given B . The final value β is the weighted mean of all the β_B indices with $\sigma \leq 0.4$ and coefficient of correlation⁴ $r^2 \geq 0.9$. The different values of β_B satisfying these conditions are consistently lower than ~ -2 , and have a weighted average and formal error $\beta = -2.3 \pm 0.2$ (see Rodón 2009 for a more detailed description of this method).

We see then that our results for the CMF slope are steeper than the ~ -1.6 found for the Clump Mass Functions (e.g., Stutzki & Guesten 1990; Kramer et al. 1998), obtained with CO emission maps for structures of sizes on the order of $\sim 0.1 \text{ pc}$. Going to at least one order of magnitude better in spatial resolution, we find that the slope of the Mass Function is consistently steeper, indicating further fragmentation at smaller spatial scales.

For reference, Figure 10 shows an example of the CMFs we obtained, in this case corresponding to $B = 0.214$ and having a power-law index $\beta = 2.3 \pm 0.2$. A turnover in the distribution at the bin centered at $\sim 1.4 M_\odot$ can be seen, containing masses above $\sim 1 M_\odot$. It appears in all the derived CMFs at about the same position, and since it matches our detection threshold, it is likely caused by the low-mass incompleteness of our sample rather than being a physical feature. In all of the cases, we fit our mass distributions for masses higher than the turnover.

The incompleteness comes both from both the sensitivity limit, as well as the crowding in the region. The sensitivity limit has been addressed in Section 3.1, giving a lower completeness limit of $\sim 1 M_\odot$. We find that the effect of crowding cannot be properly quantified with the given data. Nevertheless, in (sub)mm studies the turnover in the mass distribution and the incompleteness of the sample tend to occur at the same position (see Kirk et al. 2006, and references therein), therefore we assume that our sample is completeness-limited for masses below $\sim 1 M_\odot$.

Although we are filtering out considerable fractions of flux (section 3.1) on large spatial scales, this filtering likely affects all observations in the same way. Although we cannot draw conclusions about the absolute masses of the cores it is expected that their relative masses are correct.

⁴ This coefficient is defined as $r^2 = 1 - \frac{SS_{\text{err}}}{SS_{\text{tot}}}$, where SS_{err} is the sum of squared errors or residual sum of squares, and SS_{tot} is the total sum of squares. By this definition r^2 ranges between 0 and 1. A value of 1 means a perfect fit to the data (e.g., Draper 1998).

Table 4. CH₃CN line parameters and LTE column densities.

Source	Line	$\int T_b dv$ (K km s ⁻¹)	σ	v_c (km s ⁻¹)	σ	Width (km s ⁻¹)	σ	T_b (K)	σ	$\log N_k$ (cm ⁻²)	σ
13-s	$k = 0$	6.4	1.0	21.3	0.4	6.1	1.1	1.0	0.2	12.1	0.2
	$k = 1$	2.9	0.9	20.0	0.3	3.4	0.9	0.8	0.2	11.8	0.3
	$k = 2$	2.7	0.4	20.2	0.3	4.2	0.7	0.6	0.2	11.8	0.1
	$k = 3$	4.4	0.6	19.8	0.3	6.0	1.2	0.7	0.2	12.1	0.1
6,7,9-s	$k = 0$	2.0	0.2	22.0	0.1	1.6	0.2	1.2	0.1	11.6	0.1
	$k = 1$	1.3	0.2	20.9	0.1	1.3	0.3	0.9	0.1	11.4	0.2
4-n	$k = 0$	2.78	0.02	21.4	0.4	4.1	0.8	0.6	0.1	11.77	0.01
	$k = 1$	1.71	0.01	20.3	0.3	2.6	0.7	0.6	0.1	11.57	0.01

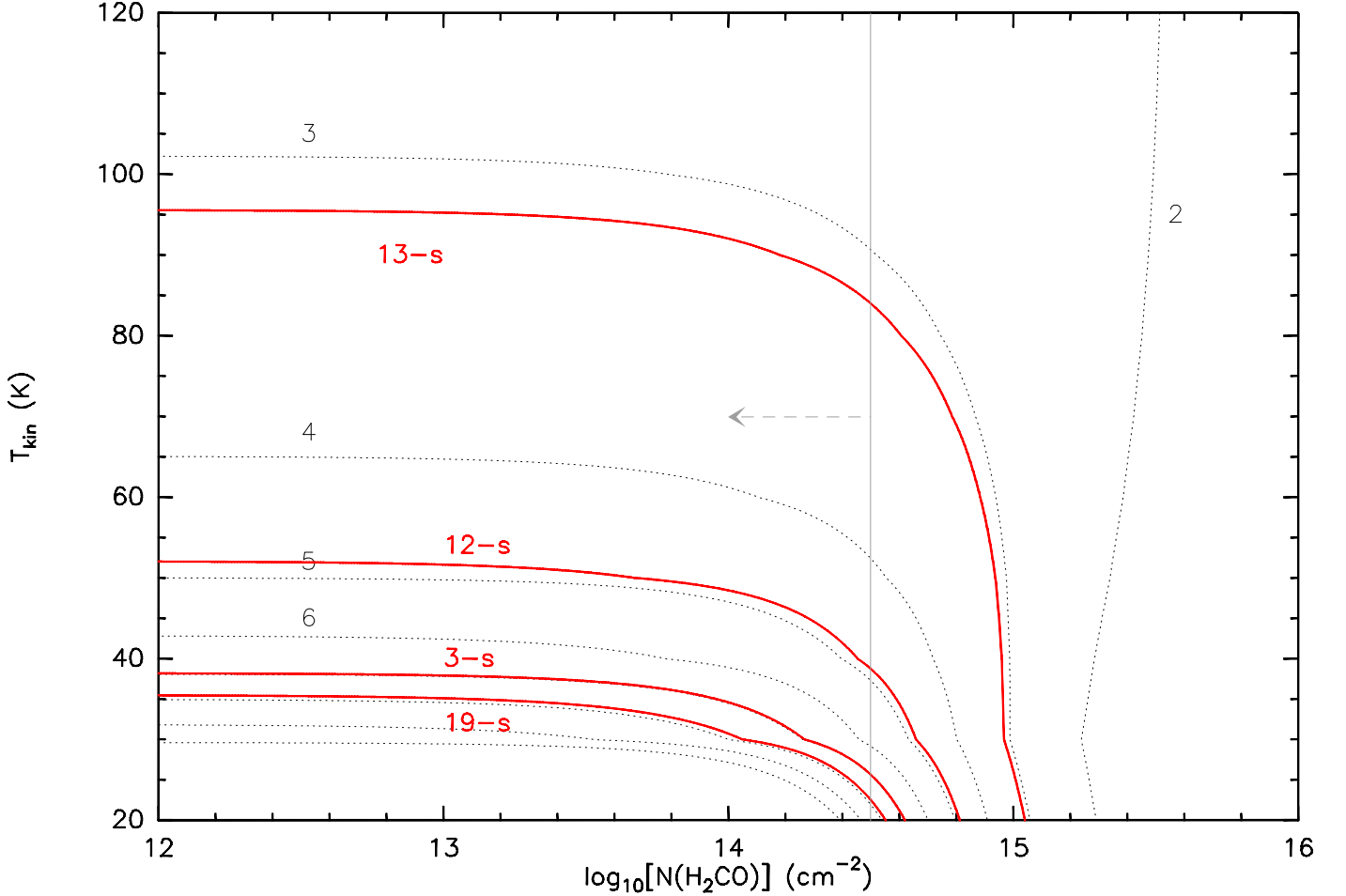


Fig. 7. Behavior of the $R = \text{H}_2\text{CO}(3_{0,3} - 2_{0,2})/\text{H}_2\text{CO}(3_{2,2} - 2_{2,1})$ integrated intensity ratio. The dotted contours represent the R values from the LVG model for $n(\text{H}_2) \sim 10^7 \text{ cm}^{-3}$ (see Sec. 4.1.2) and go from 2 to 10 in unit steps. The red solid contours are the observed R values, plotted here for cores 3-s, 12-s, 13-s and 19-s for viewing simplicity. The vertical gray dotted line is the $N(\text{H}_2\text{CO})$ upper limit value obtained with the LVG model. The effect of the optically thin/thick turnover is also seen, which introduces the largest uncertainty in the T_k estimation.

4.2.1. The Cumulative Mass Function

Using the differential CMF in a low-number sample has the disadvantage that it is sensitive to the arbitrariness of binning, as we have shown in the previous section and led to the analysis described there. On the other hand, a cumulative CMF is free from any problems associated with the binning, and is more suitable for low-number samples.

With our treatment of the CMF described in the previous section, we have taken into account the arbitrariness of the binning.

However, for comparison and further analysis we also derived a cumulative CMF for our sample. Since our differential CMF above $\sim 1 M_\odot$ can be fit by a single power-law of the form

$$\frac{\Delta N}{\Delta M} \propto M^\beta \quad (4)$$

then the cumulative CMF is

$$N(> M) \propto -\frac{1}{1+\beta} M^{1+\beta} \quad (5)$$

for $\beta < -1$. According to Reid & Wilson (2006), when using the cumulative CMF one should take into account the upper mass cutoff M_{max} of the sample, whether it is a real cutoff or a result of the finite sampling. In that case, the cumulative CMF takes the form

$$N(> M) \propto \begin{cases} \frac{1}{1+\beta} (M_{max}^{1+\beta} - M^{1+\beta}), & M < M_{max} \\ 0, & M \geq M_{max} \end{cases} \quad (6)$$

for $\beta < -1$. However, they also state that a “steep power law” ($\beta = -2.5$) will overwhelm the effect that the upper mass cutoff introduces in the fitting. From the differential CMF we see that we are close to that “steep power law” limit, so we adopt both analytical forms given in equations (5) and (6) for the cumulative CMF.

Figure 11 shows the cumulative CMF for masses above $1 M_{\odot}$. As stated before we fit both the analytical expressions given in equations (5) and (6). The results are $\beta = -2.4 \pm 0.1$ and $\beta = -2.2 \pm 0.1$, respectively, with the σ values resulting from the fitting algorithm. These results are comparable, showing that for a steep power law the inclusion of M_{max} in the definition of the cumulative CMF does not affect the result significantly (Reid & Wilson, 2006). Since both results are similar, we adopt their average value $\beta = -2.3 \pm 0.2$.

The cumulative CMF shows that the lower-mass objects dominate the fit. This is already visible in the differential CMF, but is clearer in the cumulative CMF. This is because the lower-mass bins are more populated. We see that of the 25 cores with masses above $1 M_{\odot}$ only 6 are more massive than $2.5 M_{\odot}$, therefore the lower-mass bins have more statistical weight in the fitting.

There is also an inflection in the distribution starting at $\sim 4 M_{\odot}$. It is not clear if it is a real physical feature of the distribution or a product of the uncertainty of its derivation. We discuss this in further detail in Section 5.5.

5. Discussion

5.1. Comparison with Beuther & Schilke (2004)

Beuther & Schilke (2004) detected 24 mm sources at 1.3 mm, 12 in each northern and southern cluster, with a detection threshold of $3\sigma \sim 9 \text{ mJy beam}^{-1}$. Having better sensitivity, we adopted a detection threshold of $4\sigma \sim 4 \text{ mJy beam}^{-1}$ at 1.4 mm finding 26 cores, 19 in the Southern cluster and 7 in the Northern (proto)cluster. Despite the slight difference in the total number, the general 1.4 mm high-resolution cluster structure shown in Beuther & Schilke (2004) is recovered.

This highlights the general mapping difficulties with interferometers having only a small number of antennas close to the detection limit. For example, contrary to expectations, formal 3σ limits in such maps are not as reliable as one may expect. Therefore, here we raised the threshold to 4σ . ALMA, with its many antennas, will overcome such problems.

From the analysis described in Section 4.2, we obtain a power-law CMF for IRAS 19410+2336 with an index $\beta = -2.3 \pm 0.2$, in agreement with the previous result of Beuther & Schilke (2004). The new result is more reliable than the previous one since with the new data presented here for IRAS 19410+2336 we were able to estimate a temperature structure for the (proto)clusters. Despite the limitations described in sections 4.1.2 and 5.4, that allow us to obtain a more accurate value for the core masses and thus avoid the previous caveat of assigning a uniform temperature to the whole region.

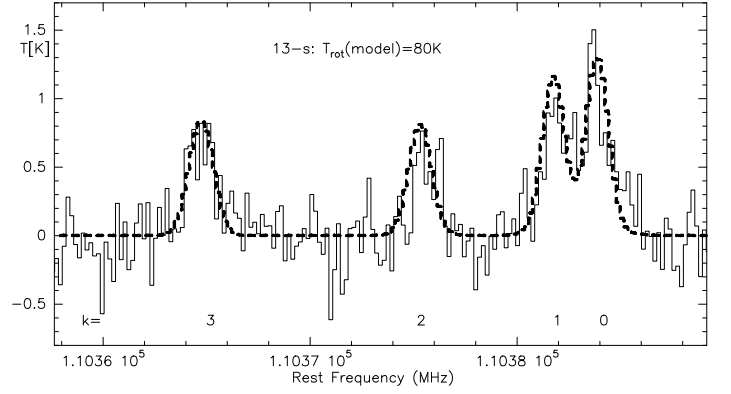


Fig. 8. XCLASS (dashed line) fit to the observed CH_3CN spectrum towards source 13-s.

Nevertheless, this similarity between the CMF indices would imply that there is not a strong dependence with the temperature structure. If we calculate the cumulative CMF of our region, but assuming a uniform temperature $T = 35 \text{ K}$, the new index is $\beta = -2.3 \pm 0.1$. In the same way, if $T = 40 \text{ K}$ then $\beta = -2.6 \pm 0.2$. Both values are indistinguishable within the errors from our main result. This feature is in part due to temperature regime. The functional dependence of the mass with the temperature implies that if we were to vary the latter from 10 K to 20 K, the mass would change by a about a factor 3. But, going to higher temperatures, the variation in mass is less pronounced. For example, a change from 40 K to 50 K implies a change in mass of less than a factor 1.5, decreasing with increasing temperatures. Our other uncertainties in the temperature and mass calculations have more weight than this effect. Nevertheless, this suggests that a detailed temperature structure plays a more significant role in the determination of the mass functions of true pre-stellar regions, because of their intrinsic lower temperatures. The calculation of the mass function of a star-forming region before its members become stars is key in determining how the parental cloud further fragments, and whether the IMF is set at the fragmentation stage or is a later result of further dynamical processes (e.g., competitive accretion, mergers, etc.).

The calculation of the power-law index was done taking into account the arbitrariness of the binning at the moment of deriving a differential CMF. Also, the cumulative CMF was taken into account in the analysis.

In the case of the cumulative CMF, the result obtained from it matches the result from the differential CMF. Although the former is better suited than the latter for the analysis of a low-number sample, in this case we observe that the fit to the cumulative CMF represents the lower-mass end of the distribution well but not the higher-mass end. However, a slight 10 K increase in temperature in the higher-mass end, which is within the uncertainty in the temperature determination, flattens the inflection seen starting at $\sim 4 M_{\odot}$, obtaining also a better fitting for the distribution while not introducing substantial modifications to the fitted parameters.

5.2. Continuum Sources

In the Southern (proto)cluster, there are NIR and MIR counterparts detected for several of our mm sources. Martín-Hernández et al. (2008) and Qiu et al. (2008) detect in the position of 13-s a bright source in the K_s filter and the $3.6\mu\text{m}$, $4.5\mu\text{m}$, $5.8\mu\text{m}$ and $8.0\mu\text{m}$ Spitzer/IRAC bands.

Martín-Hernández et al. (2008) suggest that the detected NIR and MIR emission is either leaking through an outflow-created cavity (see Beuther et al. 2003), or that the cavity itself is radiating the emission, based on their estimation that the visual extinction at that position should be very large and thus should not have any detectable NIR or even MIR emission. We confirm their estimation, finding that the visual extinction for 13-s is $A_V \sim 2700$ (see Table 2). Source 13-s is in an early stage of evolution, according to its NIR excess and the presence of H₂O and Class II CH₃OH masers (Beuther et al., 2002d), however the detection of a VLA 3.6 cm source at its position (Sridharan et al., 2002), suggest the presence of a recently ignited protostar that has already formed an Ultracompact or Hypercompact HII region, the detected radio emission being consistent with an ionizing B2 V star (Martín-Hernández et al., 2008; Qiu et al., 2008; Panagia, 1973).

In Figure 2 of Martín-Hernández et al. (2008), MIR emission is also seen at the position of the “subcluster” centered in sources 6-s, 7-s and 9-s (source mm2 in their work and in Beuther et al. 2003). There is no detected cm counterpart at that position, suggesting that either none of the sources have ignited or the ionized HII region is still too small so the free-free emission is confined and not detectable. Therefore these sources might be at an even earlier stage of evolution as 13-s, the equivalent of a Class 0 low-mass protostar, heating their circumstellar dust enough to be detected at MIR wavelengths.

Source nr76 of Martín-Hernández et al. (2008) is located less than 1.5'' from source 1-s. However, nr76 is detected in the J, H and K_s bands and not in any of the Spitzer bands, while 1-s is marginally detected at 1.4 mm and is resolved at 3 mm. The lack of emission in the Spitzer bands while being well detected in the K_s band, and the fact that is a relatively strong source at 3 mm, make us believe that nr76 is not the counterpart of 1-s, but a separate source, appearing nearby due to a projection effect.

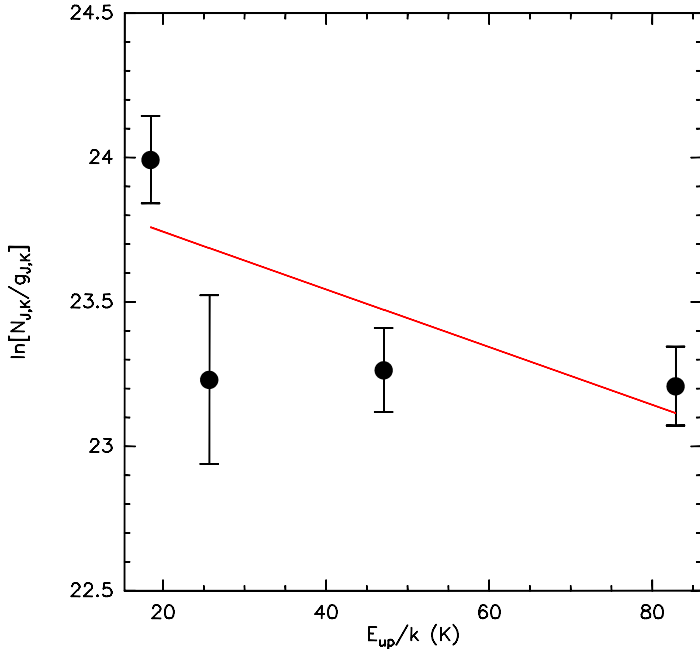


Fig. 9. Rotational diagram of the observed K -levels of $\text{CH}_3\text{CN}(J = 6 \rightarrow 5)$ towards source 13-s. The solid line is the best fit of Eq. 2, corresponding to a rotational temperature of 100 ± 60 K, in agreement with the kinetic temperature obtained with the LVG modeling of the H₂CO line emission.

The case is similar also for source nr71. It is located at $\sim 1.5''$ from 20-s, and although nr71 shows strong MIR emission, we only detect source 20-s at 3 mm and not at 1.4 mm. Therefore we believe that this is also a case of spatial projection.

This can be expected, since IRAS 19410+2336 is embedded in a cluster of Young Stellar Objects (YSOs). Martín-Hernández et al. (2008) detects 116 NIR/MIR sources in a $\sim 75'' \times 75''$ region centered on IRAS 19410+2336, while Qiu et al. (2008) detect 46 YSOs ranging from Class 0 to Class II protostars within a radius of ~ 2 pc, in addition to the detection of over 800 NIR sources in that region. The fact that there are already low-mass stars in the outskirts of IRAS 19410+2336 while high-mass stars are still forming in it supports the hypothesis that the low-mass stars form before their high-mass counterparts (e.g., Kumar et al. 2006).

Also in the Northern (proto)cluster there are identified NIR and MIR counterparts. Qiu et al. (2008) found 5-band Spitzer/IRAC and 2MASS H and K_s emission towards 4-n, as well as Spitzer/IRAC $3.6\mu\text{m}$, $4.5\mu\text{m}$, $5.8\mu\text{m}$ and $8.0\mu\text{m}$ emission towards 1/2/3-n. Source 4-n is likely at an early stage of evolution, however it is likely the most evolved source in the Northern (proto)cluster. It is not detected at cm wavelengths, therefore it has either not yet ignited its protostar or the ionized region is still too small and the free-free emission is trapped and thus not yet detectable. The other NIR/MIR detection in the (proto)cluster is towards sources 1/2/3-n, and their NIR/MIR flux is lower than that of 4-n, while their respective 1.4 mm masses are similar. This would indicate that 4-n is in a more advanced evolutionary stage than 1/2/3-n.

With a luminosity of $\sim 10^4 L_\odot$, IRAS 19410+2336 is a high-mass star-forming region, but the (proto)stellar content in its core is unknown because of high obscuration. Since it shows cm emission, most likely it already has a (proto)stellar component, ionizing an Ultra- or even a Hypercompact HII region. While it is not possible to directly measure the masses of the (proto)stars with mm data (see Sec. 3.1), it is possible to estimate the masses

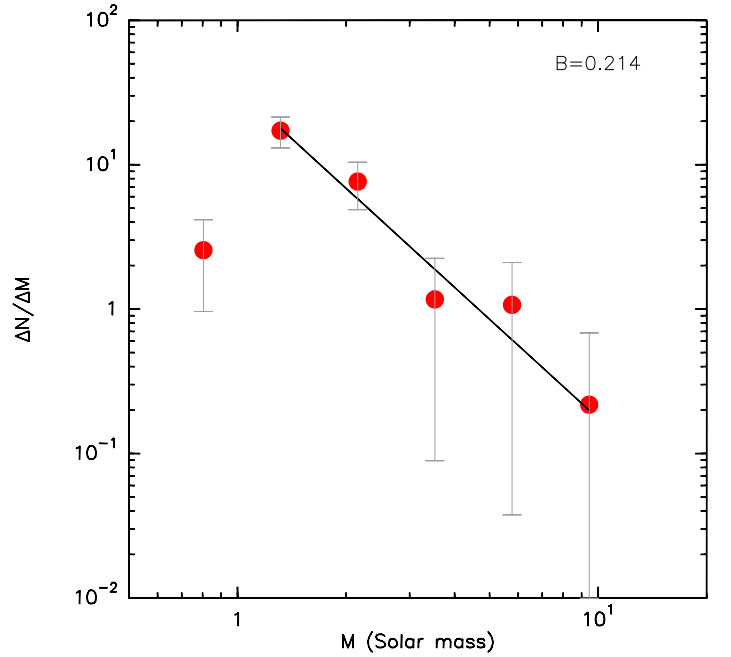


Fig. 10. Example of the CMFs obtained, corresponding to $B = 0.214$ for core masses above $1.4 M_\odot$. The solid line is the best fit of eq. (4), with a power-law index $\beta = -2.3 \pm 0.2$.

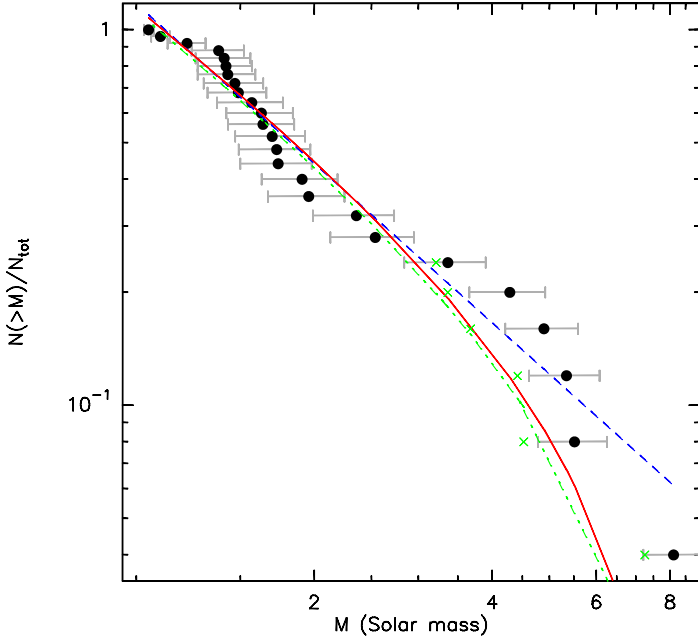


Fig. 11. Cumulative CMF of IRAS 19410+2336 for core masses above $1 M_{\odot}$. The solid red line and the dashed blue line represent the best fit of equations (6) with a power-law index $\beta = -2.2 \pm 0.1$ and (5) with $\beta = -2.4 \pm 0.1$, respectively. The green crosses represent a slight increase of 10 K in the higher-mass end, and the green dash-dotted line is the corresponding new fit of equation (6) (see Sec. 5.1). Notice the flattening of the “bump” in the distribution, while the slope of the fit practically does not change. In all cases we have normalized $N(> M)$ by the total number of cores N_{tot} .

of the circumstellar structure. Our shortest baseline of 20 m at the given distance of 2.2 kpc corresponds to a spatial scale of ~ 38000 AU at 1.4 mm, therefore any structure larger than this was not detected. Then the low masses that we calculate from the 1.4 mm data can be attributed to a circumstellar structure, while the surrounding envelope likely contributes to the larger masses derived from the 3 mm data.

5.3. Virial and Jeans analysis

The large uncertainty that the flux filtering introduces in the mass calculations can be seen when comparing the gas masses with the virial masses. The former are calculated from the interferometric continuum emission that is affected by the flux filtering, while the latter are calculated using the combined interferometric and single-dish H_2CO data, with the short-spacings correcting the effect introduced by the flux filtering. The virial and gas masses for the resolved cores in IRAS 19410+2336 are compared in Figure 12. At first glance, the cores do not appear to be collapsing, however the gas masses derived from the continuum are lower than the virial masses because of the missing flux discussed previously. If we shift the gas masses higher by a factor of 2, taking into account only $\sim 10\%$ of the missing flux, we see that within the uncertainty on the virial masses now all the resolved cores are likely collapsing.

The relative distances between neighboring cores within each (proto)cluster range several thousands of AU. These

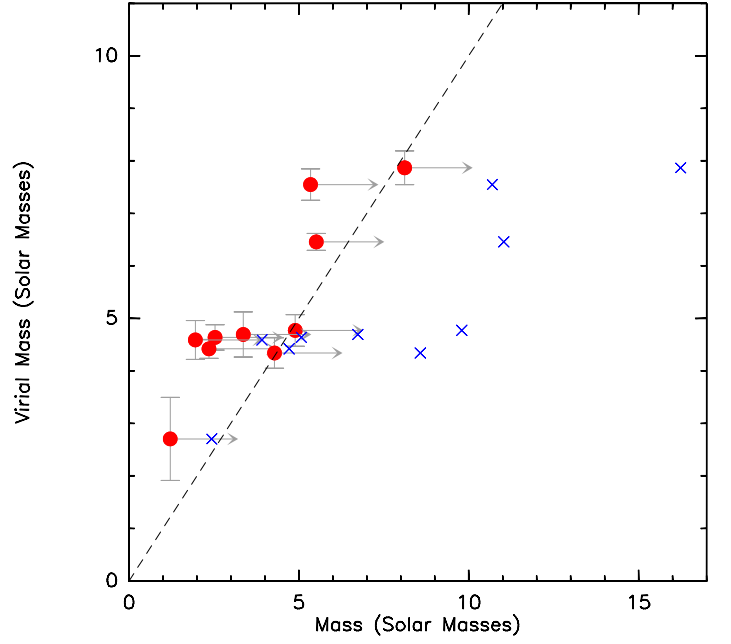


Fig. 12. Comparison between the virial masses and gas masses of the resolved cores in IRAS 19410+2336. Virial masses are not affected by the interferometric flux filtering, which does affect the gas masses. The red dots are the actual values obtained, while the blue crosses represent the relationship if we take into account $\sim 10\%$ of the flux filtered out by the interferometer. This is a hint of the care that must be taken when interpreting interferometric flux values.

are similar and below the (proto)cluster’s Jeans length $\lambda_J \sim 25000$ AU, calculated from the equation

$$\lambda_J = 0.19 \text{ pc} \left(\frac{T}{10 \text{ K}} \right)^{1/2} \left(\frac{n(\text{H}_2)}{10^4 \text{ cm}^{-3}} \right)^{-1/2} \quad (7)$$

for an average $n(\text{H}_2) \sim 10^5 \text{ cm}^{-3}$ and an average $T_k \sim 40 \text{ K}$ for the whole large-scale clumps (see Sec. 4.1.2; Stahler & Palla 2005). Our resolution of $\sim 1''$ at 1.4 mm corresponds to a spatial scale of ~ 2200 AU, which clearly resolves the Jeans length of the region. We are thus resolving the fragmentation of the clump-scale (proto)clusters far below their Jeans length. This cannot be said in the case of the cores, for which our resolution is above the Jeans length of the individual cores, in the 700 – 1200 AU range.

We are resolving the Jeans length of the clumps by one order of magnitude, almost reaching the Jeans length of the individual cores, therefore we can safely assume that we are mapping the direct progenitors of single stars or multiple systems at most (similar to the Trapezium in Orion, see e.g., Rodón et al. 2008). From the H_2CO data, we see that there is only a small signature of velocity dispersion (see Fig. 4), which would imply that the (proto)clusters are in a stage of weak dynamical evolution.

5.4. Considerations

5.4.1. Masses from (sub)mm interferometry

All interferometer observations underestimate the masses detected because of the incomplete sampling of the uv-plane. However, this filtering is not necessarily constant throughout the observed region. For instance, the single-dish observations map

the cores as well as their envelope. This gas and dust reservoir is not necessarily gravitationally bound to the cores in its totality, thus only a fraction of it will be accreted by the cores during their evolution. Theory and observations cannot yet estimate how much this fraction is, and in addition, we are not sensitive to the mass that is already in (proto)stars or in small, optically thick cores. Therefore, the underestimation factor we have calculated for the masses is an upper-limit value, obtained in the simple approximation that all the mass detected with single-dish observations is uniformly distributed and contributes to each core in the same way.

Furthermore, the cores might not draw uniformly from the envelope during their accretion phase. The competitive accretion model (e.g., Bonnell et al. 2004, 2007; Peters et al. 2010), for example, tells that the most massive cores will accrete more from the envelope than lower-mass cores, and that it cannot be pointed out to which (proto)star(s) some parts of the envelope are going to contribute. It also claims that there maybe is the problem that the mass reservoir of each (proto)star is not a well defined concept. This has then to be added to the problem of the spatial filtering from the interferometer.

All considered, we believe that the core masses we have determined are the best values that can be obtained with the currently available instruments and techniques. New studies with ALMA will certainly improve significantly in this field.

5.4.2. The nature of the CMF

In an ideal case, the CMF should be calculated with only the pre-stellar (starless) cores because if there is already a proto-star, the gas mass accreted onto it is not negligible when compared with its initial core mass. However, in the high-mass case the starless phase is very short lived if existing at all (see e.g. Motte et al. 2007). Also, some of the MSF theories propose that non-prestellar cores would not affect the resulting CMF (Clark et al. 2008, see Sec. 5.5 for more details).

We can assume a relationship of the mass function (MF) of a given region to its CMF as $CMF = f(M) * MF$, where $f(M)$ is the fraction we are able to observe. If $f(M) = const.$, then our data are a fair representation of the CMF. If it increases with mass, for example because a larger fraction is resolved out for higher-mass cores, then the slope of the MF we measure is steeper than the true CMF. If it instead decreases with Mass, because a larger fraction is resolved out for low-mass cores, the slope measured will be shallower than the true CMF. The shape of this $f(M)$ could be estimated by synthetically “observing” model CMFs. However, this is out of the scope of this paper.

Even without flux losses, unresolved substructure and projection effects complicate the picture even more.

Taking into account all these caveats, we consider that using a protostellar CMF as the one derived in this work is the best approach we can currently follow for a MSF region, though care has to be taken when comparing it with the IMF. ALMA with its much better uv-coverage and means to measure the complete flux will significantly improve our technical capabilities to study the CMF in detail.

5.5. The Core Mass Function of IRAS 19410+2336

Most of the studies that trace core scales (~ 0.01 pc) are on low-mass star forming regions, since the distances involved are of a few hundred parsecs and therefore it is possible to recover such spatial scales with single-dish telescopes. Some ex-

amples are Motte et al. (1998) and Johnstone et al. (2000), who from single-dish sub-mm observations of the ρ Ophiuchi region the authors derive in each case a mass function that resembles the IMF. A similar result is obtained by Könyves et al. (2010) with Herschel observations (i.e., in the far-IR spectrum) of the Aquila rift (see also André et al. 2010). Going up to a few solar-like masses, there are for example the works of Johnstone et al. (2006) and Nutter & Ward-Thompson (2007) on Orion. In this case, also from single-dish sub-mm observations, they recover a mass function similar to the IMF.

The mass functions of MSF regions have indeed been derived in many previous studies, however most of them with single-dish telescopes that due to the distances involved of more than ~ 2 kpc, can only recover scales on the order of 0.1 pc. According to the criteria we follow that correspond to clump scales, i.e., structures that may form (proto)clusters and not just a single star or a small multiple system. The results show mass spectra with indices β between ~ -1.2 and ~ -3 (e.g. Kramer et al. 1998; Kerton et al. 2001; Tothill et al. 2002; Shirley et al. 2003; Mookerjee et al. 2004; Reid & Wilson 2005, 2006; Beltrán et al. 2006; Muñoz et al. 2007; Ikeda & Kitamura 2011).

The case of IRAS 19410+2336 is, to our knowledge, the only one where a high-mass star forming region that could be mapped down to core scales presented enough fragmentation to derive a CMF. For a MSF region, a mass function at similar spatial scales was derived by Reid & Wilson (2005) for NGC 7538. Their smaller condensations have an average size of ~ 0.06 pc, in-between clumps and cores. In fact, they derive a mass function with a power-law index $\beta = -2.0 \pm 0.3$, which despite being comparable with the stellar IMF, is also halfway between the clump mass function value of -1.6 and the CMF value of -2.3 found in low-mass star forming regions and in this work for a MSF region.

Remarkably, IRAS 19410+2336 is a very rare object for showing more than 10 cores when resolved down to a spatial scale of several thousand AU. Similar high-spatial resolution (sub)mm observations of MSF regions typically resolve only a few cores. For example, interferometric PdBI and SMA mm mappings of the MSF regions W3 IRS 5, IRAS 06058+2138, IRAS 06061+2151, IRAS 05345+3157 and AFGL961 resolve cores down to spatial scales between ~ 750 and ~ 5000 AU, recovering in all cases fewer than 10 cores in each region (Fontani et al. 2009; Williams et al. 2009; Rodón et al. 2008; Rodón 2009). These regions are similar in distance and luminosity to IRAS 19410+2336, and although the gas mass varies, even the regions more massive than IRAS 19410+2336 show much less fragmentation at similar spatial scales. More recently, there is the work of Bontemps et al. (2010) in the Cygnus X region. They resolve 5 clumps down to spatial scales similar to the ones we obtained, recovering 23 fragments in total, from which they estimate 9 are probable high-mass protostars. Although the total number of cores is similar to this work, each clump fragments to ‘only’ 7 cores or less.

It is unclear why IRAS 19410+2336 is highly fragmented. It could be an effect of being at a different evolutionary stage, having a different chemical composition or even through perturbation and/or a different formation processes. Whichever the case, this apparent lack of fragmentation is preventing the derivation of a CMF for other individual MSF regions, highlighting the rarity of IRAS 19410+2336.

In general, observations of low-mass star-forming regions suggest that the IMF of low-mass stars is determined at early evolutionary stages (e.g., Testi & Sargent 1998; Motte et al.

1998, 2001; Alves et al. 2007; Könyves et al. 2010; see varying suggestions e.g., Goodwin & Kouwenhoven 2009). This is not so clear in the case of MSF regions, because dynamical processes like competitive accretion and merging of less massive protostars can shape the IMF at later evolutionary stages (e.g., Bonnell et al. 2004, 2007; Bonnell & Bate 2006).

A similarity between the CMF of a massive star forming region and the IMF would suggest that the structure and conditions within the molecular cloud could determine the IMF. This is essentially what was found by Chabrier & Hennebelle (2010) in a statistical study of the relationship between the CMF and the IMF. They find that both functions are correlated, and they argue that the IMF would then be defined in the early stages of evolution, being only slightly modified by environmental effects. The IMF and the CMF would also be similar if the relationship between the cores and the stars forming from them is one-to-one or nearly one-to-one. This kind of relationship is supported by theoretical models explaining the shape of the high-mass end of the IMF (e.g., Scalo et al. 1998; Padoan & Nordlund 2002), and by the apparently constant star formation efficiency suggested both by theory and observations (Matzner & McKee, 2000; Alves et al., 2007).

Also, in the Clark et al. (2008) picture of competitive accretion, the shape of the IMF is independent of when competitive accretion is halted. This would suggest that the IMF is set early on in the evolution of the clump, and therefore having non-prestellar cores at the moment of deriving a CMF would not affect the final results.

Taking into account the caveats discussed in Section 5.4, our derived power-law index β is similar to the high-mass end of the Salpeter IMF, and one would then be tempted to do a direct comparison between them. However, the CMF we derive is not completely pre-stellar, since we cannot confidently extract all the (proto)stellar sources. This means that our CMF is “contaminated” with sources that could already be considered when calculating the local IMF in the region. Thus we cannot draw solid conclusions about the likeness of the CMF of MSF regions and the IMF until the former cannot be derived with just pre-stellar cores.

Even then, caution must be taken when doing a direct comparison between the CMF and the IMF. Numerical simulations show that although the overall shape of the IMF in the low-mass to intermediate-mass regime is robust against different core evolution scenarios, further turbulent fragmentation of the cores may change the high-mass slope of the IMF (Swift & Williams, 2008).

6. Conclusions

We resolve the two clumps of the MSF region IRAS 19410+2336 into 26 cores at 1.4 mm, with a spatial resolution of ~ 2200 AU. This resolves the Jeans length of the clumps, and the relative distances between the cores are similar or smaller than the Jeans length corresponding to individual cores. Also, the cores show only a marginal signature of velocity dispersion, implying that the (proto)clusters are not in a strong dynamical evolution.

The approach of calculating temperatures using H_2CO lines might not be suitable for studies at high-spatial resolution and density like this one. We find that the H_2CO and the continuum emission only correlate for the brightest source in each (proto)cluster and not for the fainter sources, therefore preventing the derivation of the temperature of each single core.

However, it allows to derive a temperature structure for the (proto)clusters as a whole.

The temperature structure of IRAS 19410+2336 was determined from its H_2CO and CH_3CN emission allowing the estimation of a CMF. Taking into account the arbitrariness of the mass binning when deriving a mass function, we found a CMF index $\beta = -2.3 \pm 0.2$ for core masses above $\sim 1.4 M_\odot$, confirming the previous results of Beuther & Schilke (2004) with increased confidence levels.

It was not possible to determine with enough confidence the evolutionary stage of all the sources detected (i.e., whether they are pre-, proto-, or stellar sources). Because of this, the CMF we derive is not a fully pre-stellar one, and therefore it cannot be considered as a true predecessor of the stellar IMF, but a step in between a pre-stellar CMF and the IMF. An additional important caveat is the difficulty to combine continuum single-dish and interferometer data because of the vastly different bandpasses. This induces missing flux problems severely affecting the mass estimates.

To the present day, mapping of the CMF has been done mostly in low-mass star forming regions. We have shown and discussed the caveats that involve such a study in MSF regions, which in turn explains the rarity of such studies so far. Mapping a MSF region down to ~ 0.01 pc scales requires an angular resolution on the order of one arc-second for the closest regions, and tenths of arc-second if we go to larger distances. At (sub)mm wavelengths that can only be achieved with interferometry. The interferometers operating at this moment normally achieve $\sim 1''$ resolution, but to go below it is not that common. Sensitivity can become also an issue, and interferometers naturally filter out a large part of the incoming flux. When fully operational, ALMA will improve significantly on these observational limitations. Despite the difficulties and assumptions that have to be made due to these limitations, the study of the Core Mass Function of high-mass star forming regions has great usefulness for the study of the origin of the IMF. It is already seen that for low-mass stars, the IMF and the CMF are indistinguishable, suggesting the kind of relationship between them. That is yet unknown for high-mass stars and therefore it needs to be addressed, both theoretically and observationally.

Acknowledgements. J.A.R. & H.B. acknowledge support by the *Deutsche Forschungsgemeinschaft*, DFG project number BE 2578. J.A.R. also acknowledges support from the *International Max-Planck Research School for Astronomy and Cosmic Physics* at the University of Heidelberg.

References

- Alves, J., Lombardi, M., & Lada, C. J. 2007, *A&A*, 462, L17
- Anderson, L. D., Zavagno, A., Rodón, J. A., et al. 2010, *A&A*, 518, L99+
- André, P., Men'shchikov, A., Bontemps, S., et al. 2010, *A&A*, 518, L102+
- Beltrán, M. T., Brand, J., Cesaroni, R., et al. 2006, *A&A*, 447, 221
- Beuther, H., Kerp, J., Preibisch, T., Stanke, T., & Schilke, P. 2002a, *A&A*, 395, 169
- Beuther, H. & Schilke, P. 2004, *Science*, 303, 1167
- Beuther, H., Schilke, P., Menten, K. M., et al. 2002b, *ApJ*, 566, 945
- Beuther, H., Schilke, P., Menten, K. M., et al. 2005, *ApJ*, 633, 535
- Beuther, H., Schilke, P., Sridharan, T. K., et al. 2002c, *A&A*, 383, 892
- Beuther, H., Schilke, P., & Stanke, T. 2003, *A&A*, 408, 601
- Beuther, H., Walsh, A., Schilke, P., et al. 2002d, *A&A*, 390, 289
- Beuther, H., Zhang, Q., Sridharan, T. K., Lee, C.-F., & Zapata, L. A. 2006, *A&A*, 454, 221
- Bonnell, I. A. & Bate, M. R. 2006, *MNRAS*, 370, 488
- Bonnell, I. A., Larson, R. B., & Zinnecker, H. 2007, in *Protostars and Planets V*, ed. B. Reipurth, D. Jewitt, & K. Keil, 149–164
- Bonnell, I. A., Vine, S. G., & Bate, M. R. 2004, *MNRAS*, 349, 735
- Bontemps, S., Motte, F., Csengeri, T., & Schneider, N. 2010, *A&A*, 524, A18+
- Carey, S. J., Clark, F. O., Egan, M. P., et al. 1998, *ApJ*, 508, 721

- Chabrier, G. & Hennebelle, P. 2010, *ApJ*, 725, L79
- Clark, P. C., Bonnell, I. A., & Klessen, R. S. 2008, *MNRAS*, 386, 3
- Draine, B. T., Dale, D. A., Bendo, G., et al. 2007, *ApJ*, 663, 866
- Draper, N. R. 1998, *Applied regression analysis*, ed. N. R. Draper
- Fontani, F., Zhang, Q., Caselli, P., & Bourke, T. L. 2009, *A&A*, 499, 233
- Frerking, M. A., Langer, W. D., & Wilson, R. W. 1982, *ApJ*, 262, 590
- Goodwin, S. P. & Kouwenhoven, M. B. N. 2009, *MNRAS*, 397, L36
- Goodwin, S. P., Kroupa, P., Goodman, A., & Burkert, A. 2007, in *Protostars and Planets V*, ed. B. Reipurth, D. Jewitt, & K. Keil, 133–147
- Hildebrand, R. H. 1983, *QJRAS*, 24, 267
- Ikeda, N. & Kitamura, Y. 2011, *ApJ*, 732, 101
- Jansen, D. J., van Dishoeck, E. F., & Black, J. H. 1994, *A&A*, 282, 605
- Jansen, D. J., van Dishoeck, E. F., Black, J. H., Spaans, M., & Sosin, C. 1995, *A&A*, 302, 223
- Johnstone, D., Matthews, H., & Mitchell, G. F. 2006, *ApJ*, 639, 259
- Johnstone, D., Wilson, C. D., Moriarty-Schieven, G., et al. 2000, *ApJ*, 545, 327
- Kerton, C. R., Martin, P. G., Johnstone, D., & Ballantyne, D. R. 2001, *ApJ*, 552, 601
- Kirk, H., Johnstone, D., & Di Francesco, J. 2006, *ApJ*, 646, 1009
- Könyves, V., André, P., Men'shchikov, A., et al. 2010, *A&A*, 518, L106+
- Kramer, C., Stutzki, J., Rohrig, R., & Corneliussen, U. 1998, *A&A*, 329, 249
- Kroupa, P. 2002, *Science*, 295, 82
- Kumar, M. S. N., Keto, E., & Clerkin, E. 2006, *A&A*, 449, 1033
- Loren, R. B. & Mundy, L. G. 1984, *ApJ*, 286, 232
- Maíz Apellániz, J. & Ubeda, L. 2005, *ApJ*, 629, 873
- Mangum, J. G. & Wootten, A. 1993, *ApJS*, 89, 123
- Martín-Hernández, N. L., Bik, A., Puga, E., Nürnberger, D. E. A., & Bronfman, L. 2008, *A&A*, 489, 229
- Matzner, C. D. & McKee, C. F. 2000, *ApJ*, 545, 364
- Mookerjee, B., Kramer, C., Nielbock, M., & Nyman, L.-Å. 2004, *A&A*, 426, 119
- Motte, F., André, P., & Neri, R. 1998, *A&A*, 336, 150
- Motte, F., André, P., Ward-Thompson, D., & Bontemps, S. 2001, *A&A*, 372, L41
- Motte, F., Bontemps, S., Schilke, P., et al. 2007, *A&A*, 476, 1243
- Motte, F., Schilke, P., & Lis, D. C. 2003, *ApJ*, 582, 277
- Muñoz, D. J., Mardones, D., Garay, G., et al. 2007, *ApJ*, 668, 906
- Mühle, S., Seaquist, E. R., & Henkel, C. 2007, *ApJ*, 671, 1579
- Mundy, L. G., Evans, II, N. J., Snell, R. L., & Goldsmith, P. F. 1987, *ApJ*, 318, 392
- Nutter, D. & Ward-Thompson, D. 2007, *MNRAS*, 374, 1413
- Ossenkopf, V. & Henning, T. 1994, *A&A*, 291, 943
- Padoan, P. & Nordlund, Å. 2002, *ApJ*, 576, 870
- Panagia, N. 1973, *AJ*, 78, 929
- Peters, T., Klessen, R. S., Mac Low, M., & Banerjee, R. 2010, *ApJ*, 725, 134
- Qiu, K., Zhang, Q., Megeath, S. T., et al. 2008, *ApJ*, 685, 1005
- Rathborne, J. M., Jackson, J. M., Zhang, Q., & Simon, R. 2008, *ApJ*, 689, 1141
- Reid, M. A. & Wilson, C. D. 2005, *ApJ*, 625, 891
- Reid, M. A. & Wilson, C. D. 2006, *ApJ*, 644, 990
- Ridge, N. A. & Moore, T. J. T. 2001, *A&A*, 378, 495
- Rodmann, J., Henning, T., Chandler, C. J., Mundy, L. G., & Wilner, D. J. 2006, *A&A*, 446, 211
- Rodón, J. A. 2009, PhD thesis, Max-Planck-Institut für Astronomie, Heidelberg, Germany
- Rodón, J. A., Beuther, H., Megeath, S. T., & van der Tak, F. F. S. 2008, *A&A*, 490, 213
- Rodón, J. A., Zavagno, A., Baluteau, J., et al. 2010, *A&A*, 518, L80+
- Salpeter, E. E. 1955, *ApJ*, 121, 161
- Scalo, J., Vazquez-Semadeni, E., Chappell, D., & Passot, T. 1998, *ApJ*, 504, 835
- Schilke, P., Phillips, T. G., & Mehringer, D. M. 1999, in *The Physics and Chemistry of the Interstellar Medium*, ed. V. Ossenkopf, J. Stutzki, & G. Winnewisser, 330–+
- Shirley, Y. L., Evans, N. J., Young, K. E., Knez, C., & Jaffe, D. T. 2003, *ApJS*, 149, 375
- Sridharan, T. K., Beuther, H., Schilke, P., Menten, K. M., & Wyrowski, F. 2002, *ApJ*, 566, 931
- Stahler, S. W. & Palla, F. 2005, *The Formation of Stars (The Formation of Stars, by Steven W. Stahler, Francesco Palla, pp. 865. ISBN 3-527-40559-3. Wiley-VCH, January 2005.)*
- Stutzki, J. & Guesten, R. 1990, *ApJ*, 356, 513
- Swift, J. J. & Williams, J. P. 2008, *ApJ*, 679, 552
- Testi, L. & Sargent, A. I. 1998, *ApJ*, 508, L91
- Tieftunk, A. R., Gaume, R. A., & Wilson, T. L. 1998, *A&A*, 340, 232
- Tohill, N. F. H., White, G. J., Matthews, H. E., et al. 2002, *ApJ*, 580, 285
- van der Tak, F. F. S., van Dishoeck, E. F., & Caselli, P. 2000, *A&A*, 361, 327
- Watanabe, T. & Mitchell, G. F. 2008, *AJ*, 136, 1947
- Williams, J. P., Mann, R. K., Beaumont, C. N., et al. 2009, *ApJ*, 699, 1300
- Wilner, D. J., Wright, M. C. H., & Plambeck, R. L. 1994, *ApJ*, 422, 642
- Wootten, A., Evans, II, N. J., Snell, R., & vanden Bout, P. 1978, *ApJ*, 225, L143
- Xu, Y., Reid, M. J., Menten, K. M., et al. 2009, *ApJ*, 693, 413
- Zhang, Q., Ho, P. T. P., & Ohashi, N. 1998, *ApJ*, 494, 636